The Astrophysical Journal, 715:572–588, 2010 May 20 doi:10.1088/0004-637X/715/1/572

THE GREAT OBSERVATORIES ALL-SKY LIRG SURVEY: COMPARISON OF ULTRAVIOLET AND FAR-INFRARED PROPERTIES

Justin H. Howell[1], Lee Armus[1], Joseph M. Mazzarella[2], Aaron S. Evans[3,4], Jason A. Surace[1], David B. Sanders[5], Andreea Petric[1], Phil Appleton[6], Greg Bothun[7], Carrie Bridge[1,8], Ben H. P. Chan[2], Vassilis Charmandaris[9,10,11], David T. Frayer[6], Sebastian Haan[1], Hanae Inami[1], Dong-Chan Kim[3], Steven Lord[6], Barry F. Madore[2,12], Jason Melbourne[8], Bernhard Schulz[6], Vivian U[5,13], Tatjana Vavilkin[14], Sylvain Veilleux[15], and Kevin Xu[6]

[1] Spitzer Science Center, MS 220-6, California Institute of Technology, Pasadena, CA 91125, USA; jhhowell@ipac.caltech.edu
[2] Infrared Processing & Analysis Center, MS 100-22, California Institute of Technology, Pasadena, CA 91125, USA
[3] Department of Astronomy, University of Virginia, P.O. Box 400325, Charlottesville, VA 22904, USA
[4] National Radio Astronomy Observatory, 520 Edgemont Road, Charlottesville, VA 22903, USA
[5] Institute for Astronomy, University of Hawaii, 2680 Woodlawn Drive, Honolulu, HI 96822, USA
[6] NASA Herschel Science Center, IPAC, MS 100-22, California Institute of Technology, Pasadena, CA 91125, USA
[7] Department of Physics, University of Oregon, Eugene, OR 97403, USA
[8] Caltech Optical Observatories, Division of Physics, Mathematics and Astronomy, Mail Stop 320-47, California Institute of Technology, Pasadena, CA 91125, USA
[9] University of Crete, Department of Physics, Heraklion 71003, Greece
[10] IESL/Foundation for Research and Technology-Hellas, GR-71110, Heraklion, Greece
[11] Chercheur Associé, Observatoire de Paris, F-75014, Paris, France
[12] The Observatories, Carnegie Institution of Washington, 813 Santa Barbara Street, Pasadena, CA 91101, USA
[13] Harvard-Smithsonian Center for Astrophysics, 60 Garden St., Cambridge, MA 02138, USA
[14] Department of Physics and Astronomy, State University of New York at Stony Brook, Stony Brook, NY 11794-3800, USA
[15] Department of Astronomy, University of Maryland, College Park, MD 20742, USA
Received 2009 August 9; accepted 2010 April 1; published 2010 April 30

ABSTRACT

The Great Observatories All-sky LIRG Survey (GOALS) consists of a complete sample of 202 luminous infrared galaxies (LIRGs) selected from the *IRAS* Revised Bright Galaxy Sample (RBGS). The galaxies span the full range of interaction stages, from isolated galaxies to interacting pairs to late stage mergers. We present a comparison of the UV and infrared properties of 135 galaxies in GOALS observed by *GALEX* and *Spitzer*. For interacting galaxies with separations greater than the resolution of *GALEX* and *Spitzer* ($\sim$2″–6″), we assess the UV and IR properties of each galaxy individually. The contribution of the FUV to the measured star formation rate (SFR) ranges from 0.2% to 17.9%, with a median of 2.8% and a mean of 4.0% $\pm$ 0.4%. The specific star formation rate (SSFR) of the GOALS sample is extremely high, with a median value (3.9×10^{-10} yr^{-1}) that is comparable to the highest SSFRs seen in the Spitzer Infrared Nearby Galaxies Survey sample. We examine the position of each galaxy on the IR excess–UV slope (IRX–β) diagram as a function of galaxy properties, including IR luminosity and interaction stage. The LIRGs on average have greater IR excesses than would be expected based on their UV colors if they obeyed the same relations as starbursts with $L_{\rm IR} < 10^{11}\ L_{\odot}$ or normal late-type galaxies. The ratio of $L_{\rm IR}$ to the value one would estimate from the IRX–β relation published for lower luminosity starburst galaxies ranges from 0.2 to 68, with a median value of 2.7. A minimum of 19% of the total IR luminosity in the RBGS is produced in LIRGs and ultraluminous infrared galaxies with red UV colors ($\beta > 0$). Among resolved interacting systems, 32% contain one galaxy which dominates the IR emission while the companion dominates the UV emission. Only 21% of the resolved systems contain a single galaxy which dominates both wavelengths.

Key words: infrared: galaxies – ultraviolet: galaxies

1. INTRODUCTION

The *Infrared Astronomical Satellite* (*IRAS*) provided the first unbiased survey of the sky at mid- and far-infrared wavelengths, giving us a comprehensive census of the infrared emission properties of galaxies in the local universe. A major result of this survey was the discovery of a large population of luminous infrared galaxies (LIRGs) which emit a large majority of their bolometric luminosity in the far-infrared, and have $10^{11}\ L_{\odot} \leqslant L_{\rm IR}\,[8\text{–}1000\ \mu{\rm m}] < 10^{12}\ L_{\odot}$. LIRGs are a mixture of single galaxies, disk galaxy pairs, interacting systems, and advanced mergers. They exhibit enhanced star formation rates (SFRs) and a higher fraction of active galactic nuclei (AGNs) compared to less luminous and non-interacting galaxies (Sanders & Mirabel 1996, and references therein). At the highest luminosities, ultraluminous infrared galaxies (ULIRGs; $L_{\rm IR} \geqslant 10^{12}\ L_{\odot}$) may represent an important evolutionary stage in the formation of QSOs (Sanders et al. 1988a, 1988b) and massive ellipticals (e.g., Genzel et al. 2001; Tacconi et al. 2002). Since LIRGs comprise the bulk of the cosmic infrared background and dominate the star formation activity between $0.5 < z < 1$ (Le Floc'h et al. 2005; Caputi et al. 2006), they may also play a key role in our understanding of the general evolution of galaxies and black holes (e.g., Magorrian et al. 1998).

The Great Observatories All-sky LIRG Survey (GOALS; Armus et al. 2009) contains a complete sample of low-redshift LIRGs and ULIRGs with observations across the electromagnetic spectrum. The GOALS targets are drawn from the *IRAS* Revised Bright Galaxy Sample (RBGS; Sanders et al. 2003), a complete sample of 629 galaxies with *IRAS* 60 μm flux densities $S_{60} > 5.24$ Jy, covering the full sky above Galactic latitudes $|b| > 5^{\circ}$. The 629 galaxies have a median redshift of $z = 0.008$ and a maximum redshift of $z = 0.088$. There are 181 LIRGs and 21 ULIRGs in the RBGS, and these galaxies define the GOALS sample.

In LIRGs and ULIRGs, UV radiation is produced by young stars and AGN. A fraction of the UV radiation is absorbed by dust and re-radiated in the far-infrared. To understand the power sources in these galaxies, it is essential to fully characterize the energy budget by measuring both the emerging UV and the infrared flux. The relationship between the UV continuum slope and the infrared excess (the IRX–β correlation) provides a useful parameterization of this energy budget. Charlot & Fall (2000) showed that the IRX–β relation is a sequence in effective optical depth for star-forming systems. However, this relation does not hold in all systems. While lower luminosity starbursts follow the correlation, ULIRGs do not (Meurer et al. 1999; Goldader et al. 2002). The GOALS sample allows us to explore the IRX–β correlation precisely over the luminosity range where it breaks down. A detailed study of LIRGs may indicate the luminosity threshold or the time during the merger when the UV slope becomes decoupled from the IR emission. Being a flux limited sample of the nearest and most well-studied LIRGs and ULIRGs, GOALS provides an important local benchmark against which to compare the observed visual properties of high-redshift galaxies. This paper looks at global UV and IR properties. Future work will address nearby spatially resolved LIRGs.

This paper is divided into five sections. The data are discussed in Section 2. Analysis of the sample is presented in Section 3, results are discussed in Section 4, and conclusions are given in Section 5. A cosmology of $\Omega_\Lambda = 0.72$, $\Omega_m = 0.28$, with $H_0 = 70$ km s^{-1} Mpc^{-1} is adopted throughout.

2. OBSERVATIONS AND DATA REDUCTION

The GOALS *GALEX* sample consists of 135 systems observed as part of *GALEX* Cycle 1 program No. 13 (PI: Mazzarella), *GALEX* Cycle 5 program No. 38 (PI: Howell), the Nearby Galaxy Survey (NGS), and the All Sky Survey (AIS). All systems have been observed in both the FUV ($\lambda_{\rm eff} = 1528$ Å) and NUV ($\lambda_{\rm eff} = 2271$ Å). Integration times range from $\sim$100 s for the AIS data to >1500 s for the Cycle 1, Cycle 5, and NGS data. Aside from a handful of galaxies not yet observed from the Cycle 5 program, the 135 systems described here represent all GOALS targets accessible to *GALEX*.

Photometry was performed on the standard *GALEX* pipeline data products. Since *GALEX* backgrounds are very low, especially for FUV images, standard photometry codes often return a background value of zero. To accurately measure the background in these images, we followed the prescription of Gil de Paz et al. (2007, hereafter GDP) using software written by those authors and made available to us. Standard IDL aperture photometry codes were used to measure the total UV fluxes inside large apertures (typically 1′ radius) matched to *Spitzer* 24 μm MIPS photometry (J. Mazzarella et al. 2010, in preparation). Aperture centers were taken from Armus et al. (2009). The resultant UV *GALEX* photometry of the sample is presented in Table 1. In the case of widely separated pairs, only the more IR-luminous component is listed. Close pairs are treated as a single system, with the combined flux density listed in the table.

To test the accuracy of our measurements and to ensure meaningful comparisons with published data sets such as GDP, galaxies with D25 ellipses (de Vaucouleurs et al. 1991, p. 2069) were measured in D25 elliptical apertures. Little difference was found between the fluxes measured in the D25 aperture as compared to the circular aperture. The seven targets in common with the sample of GDP revealed a systematic shift in the photometric calibration between different versions of the *GALEX* data reduction pipeline. To account for this, the GDP fluxes have been adjusted for purposes of comparison with the GOALS sample. The raw count rates (before background subtraction) have been multiplied by factors of 0.89 (FUV) and 1.05 (NUV). Fluxes and magnitudes were then recalculated after background subtraction.

The resolution of *Spitzer* allows many interacting pairs or groups to be resolved into their component galaxies in the IR. For systems with separations greater than 0.″5, the 70 μm flux ratio was used to estimate the fraction of the *IRAS* $L_{\rm IR}$ coming from each galaxy. Similarly, the 24 μm flux ratio was used for systems separated by $0.''12 < d < 0.''5$, and systems which saturated at 70 μm. The latter method is inaccurate for systems in which the two galaxies have different far-IR colors, such as the Arp 299 (NGC 3690/IC 0694) system (see Charmandaris et al. 2002). A total of 93 galaxies in 44 GOALS systems have been resolved in one or both *GALEX* FUV and NUV images. Photometry of the resolved sources is presented in Table 2.

3. RESULTS

3.1. UV Luminosities and Spectral Slopes

Although selected to be IR luminous, the GOALS sample spans a wide range of UV luminosities. The FUV flux densities range from 2.4×10^{-16} to 2.9×10^{-13} erg s^{-1} cm^{-2} Å^{-1}, with a median of 7.3×10^{-15} erg s^{-1} cm^{-2} Å^{-1} and a mean of $(1.7 \pm 0.4) \times 10^{-14}$ erg s^{-1} cm^{-2} Å^{-1}. The NUV flux densities range from 6.8×10^{-16} to 2.6×10^{-13} erg s^{-1} cm^{-2} Å^{-1} with a median of 5.1×10^{-15} erg s^{-1} cm^{-2} Å^{-1} and a mean of $(1.3 \pm 0.3) \times 10^{-14}$ erg s^{-1} cm^{-2} Å^{-1}. The log of the FUV luminosities range from 8.30 to 10.33, with a median and a mean of 9.45 ± 0.04, where the luminosities are expressed in solar units, uncorrected for reddening. The log of the NUV luminosities range from 8.30 to 10.40, with a median of 9.57 and a mean of 9.64 ± 0.04. For comparison, the characteristic luminosity L_* for the present day FUV luminosity function is $10^{9.6}$ $L_\odot$ (Wyder et al. 2005). The GOALS sample is thus on average only 30% fainter than L_* in the FUV, and the most UV-luminous LIRGs in GOALS are ultraviolet luminous galaxies (UVLGs, defined as $\log(L_{\rm FUV}/L_\odot) > 10.3$; Heckman et al. 2005).

The infrared excess IRX is defined as the ratio of IR to FUV flux, most commonly expressed in logarithmic units. When calculating IRX we use $L_{\rm IR}$, the total IR luminosity from 8 to 1000 μm. $L_{\rm IR}$ is calculated using *IRAS* flux densities for integrated systems, and is allocated among resolved galaxies using MIPS flux density ratios as described above. *IRAS* flux densities for GOALS systems are taken from Sanders et al. (2003), MIPS flux densities for resolved galaxies within GOALS systems are taken from J. Mazzarella et al. (2010, in preparation), and luminosity distances are taken from Armus et al. (2009). IRX values range from 1.08 to 3.42, with a median of 2.02 and a mean of 2.06 ± 0.04. Derived quantities are presented in Table 3 for integrated systems and in Table 4 for resolved galaxies.

The UV continuum slope $\beta(GALEX)$ was calculated according to the definition of Kong et al. (2004):

$$\beta(GALEX) = \frac{\log(f_{\rm FUV}) - \log(f_{\rm NUV})}{-0.182}, \quad (1)$$

where $f_{\rm FUV}$ and $f_{\rm NUV}$ are the mean flux densities per unit wavelength. Values of $\beta(GALEX)$ range from -1.28 to 3.5, with a median of -0.16 and a mean of 0.07 ± 0.08. Since

Table 1
GOALS *GALEX* Photometry—Integrated Systems

System (1)	Alternate Name (2)	R.A. (J2000) (3)	Decl. (J2000) (4)	$\log(L_{IR})$ (5)	t_{FUV} (6)	f_ν(FUV) (7)	σ_{FUV} (8)	t_{NUV} (9)	f_ν(NUV) (10)	σ_{NUV} (11)
NGC 0023		$00^h09^m53\overset{s}{.}41$	$+25°55'25\overset{''}{.}6$	11.12	3410	1.26E-14	8.E-17	3410	1.49E-14	3.E-17
NGC 0034		$00^h11^m06\overset{s}{.}55$	$-12°06'26\overset{''}{.}3$	11.49	119	1.53E-14	4.E-16	119	1.05E-14	2.E-16
Arp 256	MCG-02-01-051-2	$00^h18^m50\overset{s}{.}40$	$-10°22'08\overset{''}{.}0$	11.48	1618	2.65E-14	2.E-16	1618	2.50E-14	6.E-17
ESO 350-IG038		$00^h36^m52\overset{s}{.}50$	$-33°33'19\overset{''}{.}0$	11.28	3356.05	3.95E-14	1.E-16	3356.05	2.31E-14	4.E-17
NGC 0232		$00^h42^m45\overset{s}{.}82$	$-23°33'40\overset{''}{.}9$	11.44	115	2.65E-15	2.E-16	115	2.37E-15	1.E-16
MCG+12-02-001		$00^h54^m03\overset{s}{.}61$	$+73°05'11\overset{''}{.}8$	11.50	112	3.60E-16	3.E-16	112	1.61E-16	1.E-16
NGC 0317B		$00^h57^m41\overset{s}{.}67$	$+43°47'33\overset{''}{.}2$	11.19	110	2.36E-15	3.E-16	110	4.29E-15	1.E-16
IC 1623	VV 114	$01^h07^m47\overset{s}{.}18$	$-17°30'25\overset{''}{.}3$	11.71	1668	6.40E-14	2.E-16	1668	4.87E-14	8.E-17
MCG-03-04-014		$01^h10^m08\overset{s}{.}96$	$-16°51'09\overset{''}{.}8$	11.65	3241	3.63E-15	5.E-17	3241	3.78E-15	2.E-17
ESO 244-G012		$01^h18^m08\overset{s}{.}10$	$-44°27'51\overset{''}{.}0$	11.38	117	8.88E-15	4.E-16	117	7.59E-15	1.E-16
CGCG 436-030		$01^h20^m02\overset{s}{.}72$	$+14°21'42\overset{''}{.}9$	11.69	3178.05	6.42E-15	6.E-17	6101.5	8.68E-15	2.E-17
IRAS F01364-1042		$01^h38^m52\overset{s}{.}92$	$-10°27'11\overset{''}{.}4$	11.85	3284	2.50E-16	3.E-17	3753	7.62E-16	1.E-17
NGC 0695		$01^h51^m14\overset{s}{.}24$	$+22°34'56\overset{''}{.}5$	11.68	3403	4.96E-15	6.E-17	6404	6.83E-15	2.E-17
UGC 01385		$01^h54^m53\overset{s}{.}79$	$+36°55'04\overset{''}{.}6$	11.05	137	1.09E-14	4.E-16	137	8.60E-15	1.E-16
NGC 0877		$02^h17^m59\overset{s}{.}64$	$+14°32'38\overset{''}{.}6$	11.10	1694	2.81E-14	2.E-16	1694	2.68E-14	6.E-17
MCG+05-06-036		$02^h23^m20\overset{s}{.}45$	$+32°11'34\overset{''}{.}2$	11.64	147	2.29E-15	2.E-16	147	3.52E-15	8.E-17
NGC 0958		$02^h30^m42\overset{s}{.}58$	$-02°56'27\overset{''}{.}2$	11.20	1696	1.41E-14	1.E-16	1696	1.27E-14	4.E-17
NGC 1068		$02^h42^m40\overset{s}{.}71$	$-00°00'47\overset{''}{.}8$	11.40	1627	2.86E-13	5.E-16	1627	2.64E-13	2.E-16
UGC 02238		$02^h46^m17\overset{s}{.}49$	$+13°05'44\overset{''}{.}4$	11.33	1316	1.42E-15	7.E-17	1400	1.28E-15	3.E-17
IRAS F02437+2122		$02^h46^m39\overset{s}{.}15$	$+21°35'10\overset{''}{.}3$	11.16	120	...	...	120	3.83E-16	9.E-17
NGC 1275		$03^h19^m48\overset{s}{.}16$	$+41°30'42\overset{''}{.}1$	11.26	14563.35	1.78E-14	5.E-17	17097.35	1.67E-14	2.E-17
NGC 1365		$03^h33^m36\overset{s}{.}37$	$-36°08'25\overset{''}{.}4$	11.00	1662.05	1.14E-13	5.E-16	1662.05	1.05E-13	2.E-16
IRAS F03359+1523		$03^h38^m46\overset{s}{.}70$	$+15°32'55\overset{''}{.}0$	11.55	107	9.11E-16	3.E-16	107	1.32E-15	6.E-17
CGCG 465-012		$03^h54^m16\overset{s}{.}08$	$+15°55'43\overset{''}{.}4$	11.20	133	3.49E-16	3.E-16	133	1.68E-15	1.E-16
IRAS 03582+6012		$04^h02^m30\overset{s}{.}65$	$+60°20'33\overset{''}{.}4$	11.43	116	...	...	116	8.08E-17	1.E-16
UGC 02982		$04^h12^m22\overset{s}{.}45$	$+05°32'50\overset{''}{.}6$	11.20	113	4.51E-16	4.E-16	113	2.46E-16	1.E-16
ESO 550-IG025		$04^h21^m20\overset{s}{.}00$	$-18°48'48\overset{''}{.}0$	11.51	129	2.68E-15	3.E-16	129	2.80E-15	1.E-16
IRAS 04271+3849		$04^h30^m33\overset{s}{.}09$	$+38°55'47\overset{''}{.}7$	11.11	166	...	...	166	...	...
ESO 203-IG001		$04^h46^m49\overset{s}{.}50$	$-48°33'32\overset{''}{.}9$	11.86	3899	7.39E-16	3.E-17	5482	6.81E-16	1.E-17
MCG-05-12-006		$04^h52^m04\overset{s}{.}96$	$-32°59'25\overset{''}{.}6$	11.17	81	1.64E-15	3.E-16	81	3.94E-15	1.E-16
CGCG 468-002		$05^h08^m20\overset{s}{.}50$	$+17°21'58\overset{''}{.}0$	11.22	118	7.51E-16	5.E-16	118	5.07E-16	1.E-16
IRAS 05083+2441		$05^h11^m25\overset{s}{.}88$	$+24°45'18\overset{''}{.}3$	11.26	111.05	2.00E-16	2.E-16	111.05	3.42E-16	6.E-17
IRAS 05129+5128		$05^h16^m56\overset{s}{.}10$	$+51°31'56\overset{''}{.}5$	11.42	130	5.33E-16	3.E-16	130	5.90E-16	1.E-16
IRAS F05189-2524		$05^h21^m01\overset{s}{.}47$	$-25°21'45\overset{''}{.}4$	12.16	2310.05	1.58E-15	8.E-17	2311.05	1.36E-15	3.E-17
IRAS 05223+1908		$05^h25^m16\overset{s}{.}50$	$+19°10'46\overset{''}{.}0$	11.65	114	...	...	114	...	...
MCG+08-11-002		$5^h40^m43\overset{s}{.}68$	$+49°41'35\overset{''}{.}4$	11.46	3368	...	...	3368	8.60E-16	2.E-17
NGC 1961		$05^h42^m04\overset{s}{.}80$	$+69°22'43\overset{''}{.}3$	11.06	3932.05	2.86E-14	1.E-16	3932.05	2.69E-14	5.E-17
UGC 03410		$06^h14^m29\overset{s}{.}63$	$+80°26'59\overset{''}{.}6$	11.10	136	3.20E-15	3.E-16	137	2.94E-15	1.E-16
NGC 2146		$06^h18^m37\overset{s}{.}71$	$+78°21'25\overset{''}{.}3$	11.12	1621	1.39E-14	1.E-16	1621	1.93E-14	6.E-17
ESO255-IG007		$6^h27^m22\overset{s}{.}64$	$-47°10'48\overset{''}{.}4$	11.90	3393	5.46E-15	6.E-17	3393	5.21E-15	2.E-17
NGC 2342		$07^h09^m18\overset{s}{.}08$	$+20°38'09\overset{''}{.}5$	11.31	111	2.54E-14	6.E-16	111	2.26E-14	2.E-16
NGC 2369		$07^h16^m37\overset{s}{.}73$	$-62°20'37\overset{''}{.}4$	11.16	105	5.13E-15	4.E-16	105	4.72E-15	1.E-16
NGC 2388		$07^h28^m53\overset{s}{.}44$	$+33°49'08\overset{''}{.}7$	11.28	1700	2.96E-14	2.E-16	1700	2.19E-14	6.E-17
MCG+02-20-003		$07^h35^m43\overset{s}{.}37$	$+11°42'33\overset{''}{.}5$	11.13	117	1.16E-14	4.E-16	117	9.14E-15	2.E-16
NGC 2623		$08^h38^m24\overset{s}{.}08$	$+25°45'16\overset{''}{.}9$	11.60	1698	5.44E-15	8.E-17	1698	4.93E-15	3.E-17
ESO 060-IG016		$8^h52^m32\overset{s}{.}03$	$-69°01'57\overset{''}{.}3$	11.82	1580	1.11E-15	1.E-16	1580	1.65E-15	4.E-17
IRAS F08572+3915		$09^h00^m25\overset{s}{.}39$	$+39°03'54\overset{''}{.}4$	12.16	1268.1	1.39E-15	6.E-17	1268.1	1.94E-15	3.E-17
IRAS 09022-3615		$09^h04^m12\overset{s}{.}70$	$-36°27'01\overset{''}{.}1$	12.31	5224	2.38E-16	6.E-17	5224	1.11E-15	2.E-17
IRAS F09111-1007		$09^h13^m38\overset{s}{.}80$	$-10°19'20\overset{''}{.}3$	12.06	2924	1.07E-15	5.E-17	19292.1	1.84E-15	8.E-18
UGC 04881		$09^h15^m55\overset{s}{.}10$	$+44°19'55\overset{''}{.}0$	11.74	3338	2.52E-15	4.E-17	3339	3.42E-15	2.E-17
UGC 05101		$09^h35^m51\overset{s}{.}65$	$+61°21'11\overset{''}{.}3$	12.01	1690	8.91E-16	5.E-17	1690	1.29E-15	2.E-17
MCG+08-18-013		$09^h36^m37\overset{s}{.}19$	$+48°28'27\overset{''}{.}7$	11.34	105	9.76E-15	4.E-16	105	6.49E-15	1.E-16
Arp 303	IC 0563-4	$09^h46^m20\overset{s}{.}60$	$+03°03'30\overset{''}{.}0$	11.23	118	4.65E-15	3.E-16	118	4.24E-15	1.E-16
NGC 3110		$10^h04^m02\overset{s}{.}11$	$-06°28'29\overset{''}{.}2$	11.37	80	1.80E-14	6.E-16	80	1.67E-14	2.E-16
ESO 374-IG032	IRAS F10038-3338	$10^h06^m04\overset{s}{.}80$	$-33°53'15\overset{''}{.}0$	11.78	4930.65	2.28E-15	5.E-17	14429.75	7.91E-15	1.E-17
IRAS F10173+0828		$10^h20^m00\overset{s}{.}22$	$+08°13'34\overset{''}{.}0$	11.86	3284.2	5.87E-18	3.E-17	6789.2	9.63E-16	1.E-17
NGC 3221		$10^h22^m19\overset{s}{.}90$	$+21°34'30\overset{''}{.}4$	11.09	107	7.79E-15	4.E-16	107	8.36E-15	2.E-16
NGC 3256		$10^h27^m51\overset{s}{.}83$	$-43°54'13\overset{''}{.}2$	11.64	1152	3.10E-14	2.E-16	1152	3.72E-14	9.E-17
ESO 264-G036		$10^h43^m07\overset{s}{.}67$	$-46°12'44\overset{''}{.}6$	11.32	109	7.74E-17	4.E-16	109	2.70E-15	1.E-16
IRAS F10565+2448		$10^h59^m18\overset{s}{.}28$	$+24°32'34\overset{''}{.}8$	12.08	1653	4.00E-16	4.E-17	1653	9.22E-16	2.E-17
MCG+07-23-019		$11^h03^m53\overset{s}{.}20$	$+40°50'57\overset{''}{.}0$	11.62	105	7.27E-15	3.E-16	3733	5.19E-15	2.E-17
CGCG 011-076		$11^h21^m12\overset{s}{.}26$	$-02°59'03\overset{''}{.}5$	11.43	106	5.90E-16	1.E-16	106	9.41E-16	6.E-17
IRAS F11231+1456	IC 2810	$11^h25^m45\overset{s}{.}05$	$+14°40'35\overset{''}{.}9$	11.64	122	1.55E-15	1.E-16	122	2.26E-15	7.E-17
NGC 3690	Arp 299	$11^h28^m32\overset{s}{.}20$	$+58°33'44\overset{''}{.}0$	11.93	103	1.19E-13	1.E-15	103	8.09E-14	4.E-16
ESO 320-G030		$11^h53^m11\overset{s}{.}72$	$-39°07'48\overset{''}{.}9$	11.17	103	3.79E-15	4.E-16	103	4.94E-15	1.E-16

Table 1
(Continued)

System (1)	Alternate Name (2)	R.A. (J2000) (3)	Decl. (J2000) (4)	log(L_{IR}) (5)	t_{FUV} (6)	f_ν(FUV) (7)	σ_{FUV} (8)	t_{NUV} (9)	f_ν(NUV) (10)	σ_{NUV} (11)
ESO 440-IG058		$12^h06^m51\overset{s}{.}90$	$-31°56'54\overset{''}{.}0$	11.43	92	2.26E-15	3.E-16	92	3.48E-15	1.E-16
IRAS F12112+0305		$12^h13^m46\overset{s}{.}00$	$+02°48'38\overset{''}{.}0$	12.36	3713	1.46E-15	3.E-17	3713	1.14E-15	2.E-17
ESO 267-G030		$12^h14^m12\overset{s}{.}84$	$-47°13'43\overset{''}{.}2$	11.25	104	2.29E-15	4.E-16	104	2.23E-15	1.E-16
NGC 4922		$13^h01^m24\overset{s}{.}90$	$+29°18'40\overset{''}{.}0$	11.38	1888.7	1.40E-15	5.E-17	3524	2.19E-15	2.E-17
CGCG 043-099		$13^h01^m50\overset{s}{.}80$	$+04°20'00\overset{''}{.}0$	11.68	137	1.69E-15	2.E-16	137	1.36E-15	8.E-17
MCG-02-33-098-9		$13^h02^m19\overset{s}{.}70$	$-15°46'03\overset{''}{.}0$	11.17	102	5.51E-15	4.E-16	112	7.11E-15	1.E-16
ESO 507-G070		$13^h02^m52\overset{s}{.}35$	$-23°55'17\overset{''}{.}7$	11.56	1251	2.02E-15	9.E-17	1251	1.99E-15	3.E-17
VV 250a		$13^h15^m35\overset{s}{.}02$	$+62°07'28\overset{''}{.}8$	11.81	103	8.66E-15	4.E-16	120	8.87E-15	1.E-16
UGC 08387		$13^h20^m35\overset{s}{.}34$	$+34°08'22\overset{''}{.}2$	11.73	119	4.13E-15	3.E-16	119	4.65E-15	1.E-16
NGC 5104		$13^h21^m23\overset{s}{.}08$	$+00°20'32\overset{''}{.}7$	11.27	113	2.97E-15	2.E-16	120	2.89E-15	1.E-16
MCG-03-34-064		$13^h22^m24\overset{s}{.}45$	$-16°43'42\overset{''}{.}4$	11.19	110	3.13E-15	3.E-16	110	3.16E-15	6.E-16
NGC 5135		$13^h25^m44\overset{s}{.}06$	$-29°50'01\overset{''}{.}2$	11.30	108	1.80E-14	6.E-16	108	1.96E-14	2.E-16
IC 4280		$13^h32^m53\overset{s}{.}40$	$-24°12'25\overset{''}{.}7$	11.15	116	9.92E-15	4.E-16	116	1.17E-14	2.E-16
NGC 5256		$13^h38^m17\overset{s}{.}50$	$+48°16'37\overset{''}{.}0$	11.56	111	1.02E-14	4.E-16	111	9.45E-15	2.E-16
Arp 240	NGC 5257-8	$13^h39^m55\overset{s}{.}20$	$+00°50'13\overset{''}{.}0$	11.62	129	3.94E-14	7.E-16	130	3.08E-14	2.E-16
UGC 08739		$13^h49^m13\overset{s}{.}93$	$+35°15'26\overset{''}{.}8$	11.15	59	6.46E-15	4.E-16	59	4.76E-15	2.E-16
NGC 5331		$13^h52^m16\overset{s}{.}20$	$+02°06'16\overset{''}{.}0$	11.66	2704	5.21E-15	6.E-17	4312.5	5.23E-15	2.E-17
Arp 84	NGC 5394-5	$13^h58^m35\overset{s}{.}80$	$+37°26'20\overset{''}{.}0$	11.08	91	7.52E-15	4.E-16	1476	8.88E-15	4.E-17
CGCG 247-020		$14^h19^m43\overset{s}{.}25$	$+49°14'11\overset{''}{.}7$	11.39	105	4.67E-16	2.E-16	105	3.59E-16	7.E-17
NGC 5653		$14^h30^m10\overset{s}{.}42$	$+31°12'55\overset{''}{.}8$	11.13	92	1.84E-14	6.E-16	92	1.85E-14	2.E-16
IRAS F14348-1447		$14^h37^m38\overset{s}{.}37$	$-15°00'22\overset{''}{.}8$	12.39	1942	1.32E-15	7.E-17	3134	9.46E-16	2.E-17
NGC 5734		$14^h45^m09\overset{s}{.}05$	$-20°52'13\overset{''}{.}7$	11.15	128	1.06E-14	4.E-16	128	9.61E-15	2.E-16
VV 340a		$14^h57^m00\overset{s}{.}68$	$+24°37'02\overset{''}{.}7$	11.74	3042	5.72E-15	6.E-17	6028	4.89E-15	2.E-17
CGCG 049-057		$15^h13^m13\overset{s}{.}10$	$+07°13'31\overset{''}{.}8$	11.35	88	7.87E-17	2.E-16	88	9.31E-16	9.E-17
VV 705		$15^h18^m06\overset{s}{.}34$	$+42°44'36\overset{''}{.}7$	11.92	110	5.23E-15	3.E-16	110	4.14E-15	1.E-16
IRAS F15250+3608		$15^h26^m59\overset{s}{.}40$	$+35°58'37\overset{''}{.}5$	12.08	168	2.42E-15	2.E-16	1601	2.25E-15	2.E-17
NGC 5936		$15^h30^m00\overset{s}{.}84$	$+12°59'21\overset{''}{.}5$	11.14	106	2.38E-14	6.E-16	106	2.01E-14	2.E-16
UGC 09913	Arp 220	$15^h34^m57\overset{s}{.}11$	$+23°30'11\overset{''}{.}5$	12.28	92	2.02E-15	3.E-16	92	3.07E-15	8.E-17
NGC 5990		$15^h46^m16\overset{s}{.}37$	$+02°24'55\overset{''}{.}7$	11.13	109	1.08E-14	4.E-16	109	9.97E-15	2.E-16
NGC 6052		$16^h05^m12\overset{s}{.}90$	$+20°32'32\overset{''}{.}0$	11.09	97	3.71E-14	8.E-16	2137	2.70E-14	5.E-17
NGC 6090		$16^h11^m40\overset{s}{.}70$	$+52°27'24\overset{''}{.}0$	11.58	2383	1.38E-14	1.E-16	14866.05	1.28E-14	1.E-17
IRAS F16164-0746		$16^h19^m11\overset{s}{.}76$	$-07°54'04\overset{''}{.}5$	11.62	3878	1.51E-15	1.E-16	3878	1.26E-15	3.E-17
CGCG 052-037		$16^h30^m56\overset{s}{.}54$	$+04°04'58\overset{''}{.}4$	11.45	115	1.55E-15	2.E-16	115	1.85E-15	9.E-17
NGC 6240		$16^h52^m58\overset{s}{.}89$	$+02°24'03\overset{''}{.}4$	11.93	108	6.39E-15	5.E-16	17086.45	6.40E-15	1.E-17
NGC 6286		$16^h58^m31\overset{s}{.}38$	$+58°56'10\overset{''}{.}5$	11.37	122	7.32E-15	3.E-16	122	6.46E-15	1.E-16
IRAS F17132+5313		$17^h14^m20\overset{s}{.}00$	$+53°10'30\overset{''}{.}0$	11.96	3116.75	1.44E-15	4.E-17	5577.65	1.67E-15	1.E-17
IRAS F17207-0014		$17^h23^m22\overset{s}{.}16$	$-00°17'01\overset{''}{.}7$	12.46	4345	1.19E-17	4.E-17	4345	8.07E-17	1.E-17
UGC 11041		$17^h54^m51\overset{s}{.}82$	$+34°46'34\overset{''}{.}4$	11.11	114	4.74E-15	3.E-16	114	3.76E-15	1.E-16
CGCG 141-034		$17^h56^m56\overset{s}{.}63$	$+24°01'01\overset{''}{.}6$	11.20	112	1.01E-15	3.E-16	112	5.26E-16	1.E-16
NGC 6621		$18^h12^m55\overset{s}{.}31$	$+68°21'48\overset{''}{.}4$	11.29	102	5.64E-15	3.E-16	102	6.14E-15	1.E-16
IC 4687		$18^h13^m39\overset{s}{.}63$	$-57°43'31\overset{''}{.}3$	11.62	145	1.74E-14	4.E-16	145	1.43E-14	2.E-16
NGC6670AB		$18^h33^m35\overset{s}{.}60$	$+59°53'20\overset{''}{.}0$	11.65	2760	3.06E-15	6.E-17	3531	3.29E-15	2.E-17
IC 4734		$18^h38^m25\overset{s}{.}70$	$-57°29'25\overset{''}{.}6$	11.35	112	8.06E-15	4.E-16	112	6.02E-15	1.E-16
ESO 593-IG008		$19^h14^m30\overset{s}{.}90$	$-21°19'07\overset{''}{.}0$	11.93	82	2.51E-15	5.E-16	4422	5.54E-15	3.E-17
IRAS F19297-0406		$19^h32^m21\overset{s}{.}25$	$-03°59'56\overset{''}{.}3$	12.45	98.75	1.72E-17	7.E-18	3802	2.06E-17	4.E-18
ESO 339-G011		$19^h57^m37\overset{s}{.}54$	$-37°56'08\overset{''}{.}4$	11.20	113	2.08E-15	3.E-16	113	2.86E-15	1.E-16
NGC 6907		$20^h25^m06\overset{s}{.}65$	$-24°48'33\overset{''}{.}5$	11.11	1686	8.18E-14	3.E-16	2175	6.30E-14	8.E-17
NGC 6926		$20^h33^m06\overset{s}{.}11$	$-02°01'39\overset{''}{.}0$	11.32	119	1.41E-14	5.E-16	119	1.02E-14	2.E-16
CGCG 448-020	II Zw 096	$20^h57^m23\overset{s}{.}29$	$+17°07'34\overset{''}{.}3$	11.94	66	1.64E-14	6.E-16	66	1.02E-14	2.E-16
ESO 286-IG019		$20^h58^m26\overset{s}{.}79$	$-42°39'00\overset{''}{.}3$	12.06	2974	5.51E-15	6.E-17	8100.05	5.06E-15	1.E-17
ESO 286-G035		$21^h04^m11\overset{s}{.}18$	$-43°35'33\overset{''}{.}0$	11.20	105	4.35E-15	3.E-16	105	4.72E-15	1.E-16
ESO 343-IG013		$21^h36^m11\overset{s}{.}00$	$-38°32'37\overset{''}{.}0$	11.14	81	3.95E-15	3.E-16	81	4.24E-15	1.E-16
NGC 7130		$21^h48^m19\overset{s}{.}50$	$-34°57'04\overset{''}{.}7$	11.42	1692	2.11E-14	1.E-16	1692	2.42E-14	6.E-17
IC 5179		$22^h16^m09\overset{s}{.}10$	$-36°50'37\overset{''}{.}4$	11.24	86	3.36E-14	8.E-16	86	3.17E-14	3.E-16
ESO 602-G025		$22^h31^m25\overset{s}{.}48$	$-19°02'04\overset{''}{.}1$	11.34	62	3.63E-15	4.E-16	62	3.38E-15	2.E-16
UGC 12150		$22^h41^m12\overset{s}{.}26$	$+34°14'57\overset{''}{.}0$	11.35	167	9.13E-17	2.E-16	167	8.54E-16	8.E-17
IRAS F22491-1808		$22^h51^m49\overset{s}{.}26$	$-17°52'23\overset{''}{.}5$	12.20	1696	1.89E-15	6.E-17	1696	2.04E-15	3.E-17
NGC 7469		$23^h03^m15\overset{s}{.}62$	$+08°52'26\overset{''}{.}4$	11.65	3768	4.50E-14	1.E-16	3768	3.29E-14	4.E-17
CGCG 453-062		$23^h04^m56\overset{s}{.}53$	$+19°33'08\overset{''}{.}0$	11.38	113	7.51E-16	2.E-16	113	1.29E-15	9.E-17
ESO 148-IG002		$23^h15^m46\overset{s}{.}78$	$-59°03'15\overset{''}{.}6$	12.06	3009.05	5.88E-15	6.E-17	5350.05	5.22E-15	2.E-17
IC 5298		$23^h16^m00\overset{s}{.}70$	$+25°33'24\overset{''}{.}1$	11.60	113	2.21E-15	3.E-16	113	1.76E-15	1.E-16
NGC 7552		$23^h16^m10\overset{s}{.}77$	$-42°35'05\overset{''}{.}4$	11.11	4825	7.33E-14	1.E-16	7560.95	8.68E-14	5.E-17
NGC 7592		$23^h18^m22\overset{s}{.}54$	$-04°24'58\overset{''}{.}5$	11.40	107	2.32E-14	6.E-16	107	1.38E-14	2.E-16
ESO 077-IG014		$23^h21^m04\overset{s}{.}30$	$-69°12'54\overset{''}{.}0$	11.76	2060	5.34E-16	5.E-17	6625.05	1.03E-15	1.E-17
NGC 7674		$23^h27^m56\overset{s}{.}72$	$+08°46'44\overset{''}{.}5$	11.56	1666	1.42E-14	1.E-16	1666	1.16E-14	4.E-17

Table 1
(Continued)

System (1)	Alternate Name (2)	R.A. (J2000) (3)	Decl. (J2000) (4)	log(L_{IR}) (5)	t_{FUV} (6)	f_ν(FUV) (7)	σ_{FUV} (8)	t_{NUV} (9)	f_ν(NUV) (10)	σ_{NUV} (11)
IRAS F23365+3604		$23^h39^m01\overset{s}{.}27$	$+36°21'08\overset{''}{.}7$	12.20	3876	6.02E-16	5.E-17	3876	2.62E-15	2.E-17
MCG-01-60-022		$23^h41^m54\overset{s}{.}10$	$-03°38'29\overset{''}{.}0$	11.27	1489	7.28E-15	9.E-17	1489	5.50E-15	3.E-17
Arp 86	NGC 7752-3	$23^h47^m01\overset{s}{.}63$	$+29°28'17\overset{''}{.}2$	11.07	1687.7	1.02E-14	1.E-16	3246	9.15E-15	3.E-17
NGC 7771		$23^h51^m24\overset{s}{.}88$	$+20°06'42\overset{''}{.}6$	11.40	8579	3.39E-14	8.E-17	16457	2.35E-14	2.E-17
MRK0331		$23^h51^m26\overset{s}{.}80$	$+20°35'09\overset{''}{.}9$	11.50	1129	2.91E-15	1.E-16	1129	3.07E-15	4.E-17

Note. Column 1: system name, following the naming convention of Armus et al. (2009); Column 2: alternate system name; Column 3: the best available source right ascension (J2000) in NED as of 2008 October; Column 4: the best available source declination (J2000) in NED as of 2008 October; Column 5: the total infrared luminosity in $\log_{10}$ Solar units computed using the *IRAS* flux densities reported in the RBGS and the luminosity distances in Armus et al. (2009); Column 6: *GALEX* FUV integration time in seconds; Column 7: *GALEX* FUV flux density in units of erg s^{-1} cm^{-2} $Å^{-1}$; Column 8: *GALEX* FUV flux density uncertainty; Column 9: *GALEX* NUV integration time in seconds; Column 10: *GALEX* NUV flux density in units of erg s^{-1} cm^{-2} $Å^{-1}$; Column 11: *GALEX* NUV flux density uncertainty.

the *GALEX* filters have different effective wavelengths than previous instruments such as *IUE* or STIS, the normalization of $\beta(GALEX)$ is different from previous work (e.g., Meurer et al. 1999; Goldader et al. 2002; see the Appendix for a more detailed discussion and a direct conversion between $\beta(GALEX)$ and $\beta(IUE)$). Of the 135 observed systems, 112 have good quality data ($\sigma_{\beta(GALEX)} < 0.5$) and are used in the subsequent analysis. Eleven galaxies in the Meurer et al. (1999) sample are included in GDP. These systems allow us to recreate the linear portion of the IRX–$\beta(GALEX)$ relation for (sub-LIRG) starburst galaxies, hereafter referred to as the starburst relation. The 11 Meurer et al. (1999) systems in GDP span a range of $-1 < \beta(GALEX) < 0.5$, and extrapolations beyond that range are not necessarily correct.

The IRX–$\beta(GALEX)$ plot is shown in Figure 1. As Goldader et al. (2002) discovered, IR-luminous systems tend to lie above the starburst relation. Similarly, as seen in Kong et al. (2004), Cortese et al. (2006), and GDP, the starburst relation forms an upper envelope for normal galaxies on this plot. Within the valid range for the starburst relation, 15% of LIRGs fall below the relation. In addition, 12 LIRGs with very red UV colors ($\beta > 1$) have high IRX values (2.2–3.3) but lie far below a linear extrapolation to the starburst relation. The fit to the late-type galaxy sample of Cortese et al. (2006) provides a particularly clean separation between (U)LIRGs and sub-LIRGs in Figure 1. The shallower slope better matches the distributions of GOALS subpopulations ($L_{IR} < 10^{11.4}$, $10^{11.4} < L_{IR} < 10^{11.8}$, and $L_{IR} > 10^{11.8}$), with the more luminous subpopulations having larger separations in IRX from the Cortese relation. The best fit slope for the GOALS data is IRX = (0.46 ± 0.06)β + (2.1 ± 0.1), shallower than the Cortese relation by 0.24 but offset to higher IRX by 0.8 at $\beta = 0$.

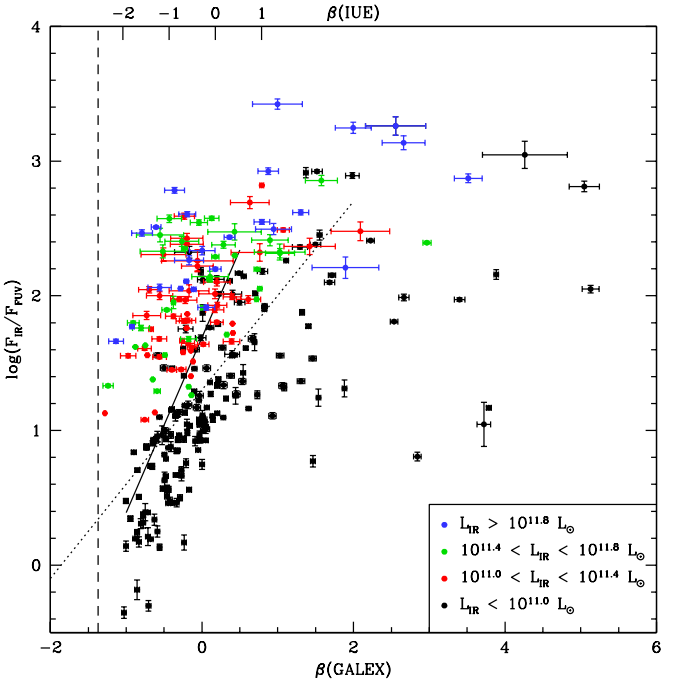

Figure 1. IR excess, F_{IR}/F_{FUV}, plotted against the UV continuum slope, $\beta(GALEX)$. Black points (from GDP) have $L_{IR} < 10^{11}$ $L_\odot$, red points have 10^{11} $L_\odot < L_{IR} < 10^{11.4}$ $L_\odot$, green points have $10^{11.4}$ $L_\odot < L_{IR} < 10^{11.8}$ $L_\odot$, and blue points have $L_{IR} > 10^{11.8}$ $L_\odot$. The solid line is a fit to the starburst galaxies of Meurer et al. (1999) which were included in the GDP sample. The dotted line is the fit to the late-type galaxy sample of Cortese et al. (2006). The vertical dashed line is the UV color of a Starburst99 (Leitherer et al. 1999) model of a 10^8 yr old starburst population with solar metallicity and a Salpeter IMF (Salpeter 1955). The range of $\beta(GALEX)$ in the *IUE* system of Meurer et al. (1999) is shown at top. Low and medium luminosity LIRGs (red and green points) fill parameter space between normal galaxies and high luminosity LIRGs and ULIRGs (blue points).

3.2. Star Formation Rates

The combination of *IRAS* L_{IR} and *GALEX* FUV measurements provides an estimate of the total (obscured plus unobscured) SFR (Kennicutt 1998; Dale et al. 2007). The contribution of the FUV to the measured SFR ranges from 0.2% to 17.9%, with a median of 2.8% and a mean of 4.0% ± 0.4%. A histogram showing the ratio of UV-derived SFR to that derived from the combination of UV and IR luminosity is shown in Figure 2(a). Calculations relating to SFR do not include galaxies with IRAC colors that are consistent with the presence of a strong AGN (Stern et al. 2005). The distribution of the FUV contribution to SFR is consistent with previous work (Surace & Sanders 2000; Surace et al. 2000). The FUV contribution to SFR is small for LIRGs and ULIRGs, and decreases as L_{IR} increases (Figure 2(b)). The Spearman rank correlation coefficient $r_s = -0.47$, with significance 3.6×10^{-6} indicating a significant correlation, although the relation is clearly nonlinear. Galaxies with larger infrared luminosity have a higher fraction of their measured star formation emerging in the far-infrared, with a corresponding lower fraction emerging in the far-ultraviolet. As a function of IR luminosity, the median (mean) contribution of the FUV to the measured SFR is 3.3% (4.6%) for systems with $L_{IR} < 10^{11.8}$, and drops to 1.9% (2.0%) for systems with $L_{IR} > 10^{11.8}$.

IRAC 3.6 μm and Two Micron All Sky Survey (2MASS) K-band photometry were used to estimate the stellar mass of each galaxy (Lacey et al. 2008). The mass estimates

Table 2
GALEX Photometry—Resolved Components

System Name (1)	Galaxy Name (2)	R.A. (J2000) (3)	Decl. (J2000) (4)	$\log(L_{IR})$ (5)	f_ν(FUV) (6)	σ_{FUV} (7)	f_ν(NUV) (8)	σ_{NUV} (9)
GOALS J001108.5-120351	NGC 0034	$00^h11^m06^s.56$	$-12°06'28''.2$	11.34	1.53E-14	4.E-16	1.05E-14	6.E-16
GOALS J001108.5-120351	NGC 0035	$00^h11^m10^s.51$	$-12°01'14''.9$	10.57	6.92E-15	3.E-16	8.63E-15	6.E-16
MCG-02-01-051-2	MCG-02-01-052	$00^h18^m49^s.85$	$-10°21'34''.0$	10.36	1.24E-14	1.E-16	1.05E-14	1.E-16
MCG-02-01-051-2	MCG-02-01-051	$00^h18^m50^s.90$	$-10°22'36''.7$	11.45	1.42E-14	1.E-16	1.08E-14	1.E-16
NGC 0232	NGC 0232	$00^h42^m45^s.83$	$-23°33'41''.0$	11.37	2.65E-15	2.E-16	2.37E-15	5.E-16
NGC 0232	NGC 0235A	$00^h42^m52^s.82$	$-23°32'27''.8$	10.86	1.28E-15	2.E-16	1.19E-15	5.E-16
NGC 0317	NGC 0317A	$00^h57^m39^s.04$	$+43°48'03''.1$	8.96	2.48E-16	3.E-17	1.37E-15	4.E-17
NGC 0317	NGC 0317B	$00^h57^m40^s.41$	$+43°47'32''.5$	11.19	2.12E-15	3.E-16	2.91E-15	9.E-17
IC 1623	IC 1623A	$01^h07^m46^s.75$	$-17°30'26''.2$	11.08	6.16E-14	2.E-16	4.57E-14	7.E-17
IC 1623	IC 1623B	$01^h07^m47^s.54$	$-17°30'25''.1$	11.59	2.31E-15	8.E-18	3.03E-15	5.E-18
ESO 244-G012	ESO 244-G012 NED01	$01^h18^m08^s.23$	$-44°28'00''.4$	9.49	7.27E-15	3.E-16	5.61E-15	1.E-16
ESO 244-G012	ESO 244-G012 NED02	$01^h18^m08^s.31$	$-44°27'43''.4$	11.37	1.61E-15	6.E-17	1.98E-15	3.E-17
GOALS J015457.8+365508	UGC 01385	$01^h54^m53^s.82$	$+36°55'04''.3$	11.00	1.92E-15	2.E-16	1.71E-15	3.E-16
GOALS J015457.8+365508	KUG 0152+366	$01^h55^m01^s.75$	$+36°55'11''.6$	10.05	8.94E-15	3.E-16	6.89E-15	4.E-16
GOALS J021756.5+143158	NGC 0876	$02^h17^m53^s.26$	$+14°31'18''.4$	10.51	2.81E-14	2.E-16	2.68E-14	2.E-16
GOALS J021756.5+143158	NGC 0877	$02^h17^m59^s.68$	$+14°32'38''.2$	11.07	1.27E-15	6.E-17	1.31E-15	2.E-16
MRK1034	MCG+05-06-035	$02^h23^m18^s.97$	$+32°11'18''.5$	11.00	1.61E-15	1.E-16	2.53E-15	6.E-17
MRK1034	MCG+05-06-036	$02^h23^m21^s.99$	$+32°11'48''.8$	11.53	6.80E-16	5.E-17	9.82E-16	2.E-17
KPG 095	UGC 02894	$03^h54^m07^s.67$	$+15°59'24''.3$	10.81	1.56E-15	3.E-16	1.36E-15	7.E-16
KPG 095	CGCG 465-012	$03^h54^m15^s.95$	$+15°55'43''.4$	11.16	3.49E-16	3.E-16	1.68E-15	7.E-16
ESO 550-IG025	ESO 550-IG025 NED01	$04^h21^m20^s.02$	$-18°48'39''.6$	11.27	2.18E-15	2.E-16	2.17E-15	8.E-17
ESO 550-IG025	ESO 550-IG025 NED02	$04^h21^m20^s.08$	$-18°48'57''.4$	11.13	5.00E-16	5.E-17	6.30E-16	2.E-17
CGCG 468-002	CGCG 468-002 NED01	$05^h08^m19^s.71$	$+17°21'47''.8$	10.74	4.20E-17	3.E-17	2.65E-16	7.E-17
CGCG 468-002	CGCG 468-002 NED02	$05^h08^m21^s.21$	$+17°22'08''.0$	11.05	7.09E-16	4.E-16	2.42E-16	6.E-17
GOALS J051127.4+244539	IRAS 05083+2441	$05^h11^m25^s.88$	$+24°45'18''.2$	11.24	1.99E-16	2.E-16	3.15E-16	4.E-16
GOALS J051127.4+244539	2MASX J05112888+2445593	$05^h11^m29^s.05$	$+24°46'04''.0$	10.06	1.02E-18	2.E-16	2.66E-17	4.E-16
KPG 108	UGC 03405	$06^h13^m57^s.90$	$+80°28'34''.7$	10.54	3.20E-15	3.E-16	2.94E-15	5.E-16
KPG 108	UGC 03410	$06^h14^m29^s.61$	$+80°26'59''.6$	11.02	1.04E-15	2.E-16	1.12E-15	5.E-16
KPG 125	NGC 2341	$07^h09^m12^s.01$	$+20°36'11''.2$	11.11	4.98E-15	4.E-16	6.98E-15	8.E-16
KPG 125	NGC 2342	$07^h09^m18^s.07$	$+20°38'10''.2$	11.20	2.54E-14	6.E-16	2.26E-14	9.E-16
WBL 142	NGC 2385	$07^h28^m28^s.17$	$+33°50'16''.9$	9.59	3.22E-16	6.E-17	1.86E-15	2.E-16
WBL 142	NGC 2388	$07^h28^m53^s.44$	$+33°49'07''.8$	11.26	2.96E-14	2.E-16	2.19E-14	2.E-16
WBL 142	NGC 2389	$07^h29^m04^s.59$	$+33°51'38''.0$	10.65	7.20E-17	6.E-17	3.62E-16	2.E-16
GOALS J073542.4+113938	NGC 2416	$07^h35^m41^s.53$	$+11°36'42''.1$	...	1.16E-14	4.E-16	9.14E-15	7.E-16
GOALS J073542.4+113938	MCG+02-20-003	$07^h35^m43^s.44$	$+11°42'34''.8$	...	5.73E-15	3.E-16	7.78E-15	7.E-16
IRAS F09111-1007	2MASX J09133644-1019296	$09^h13^m36^s.50$	$-10°19'29''.7$	11.90	3.10E-17	1.E-17	9.30E-17	8.E-18
IRAS F09111-1007	2MASX J09133888-1019196	$09^h13^m38^s.89$	$-10°19'19''.6$	11.24	1.10E-15	3.E-17	1.75E-15	4.E-19
UGC 04881	UGC 04881 NED02	$09^h15^m54^s.69$	$+44°19'50''.8$	11.26	6.89E-17	6.E-18	9.72E-17	3.E-18
UGC 04881	UGC 04881 NED01	$09^h15^m55^s.52$	$+44°19'57''.4$	11.56	1.69E-16	9.E-18	2.34E-16	4.E-18
CGCG 239-011	CGCG 239-011 NED01	$09^h36^m30^s.86$	$+48°28'09''.9$	9.93	6.88E-15	3.E-16	3.84E-15	3.E-16
CGCG 239-011	MCG+08-18-013	$09^h36^m37^s.20$	$+48°28'27''.7$	11.32	2.88E-15	2.E-16	2.65E-15	3.E-16
GOALS J112110.3-025922	2MASX J11210825-0259399	$11^h21^m08^s.29$	$-02°59'39''.2$	10.02	2.98E-16	1.E-16	2.40E-16	3.E-16
GOALS J112110.3-025922	CGCG 011-076	$11^h21^m12^s.24$	$-02°59'02''.5$	11.41	2.92E-16	1.E-16	7.01E-16	3.E-16
IC 2810	IC 2810A	$11^h25^m45^s.07$	$+14°40'36''.0$	11.45	1.43E-15	1.E-16	2.10E-15	3.E-16
IC 2810	IC 2810B	$11^h25^m49^s.55$	$+14°40'06''.6$	11.20	1.28E-16	7.E-17	1.62E-16	2.E-16
Arp 299	NGC 3690	$11^h28^m31^s.04$	$+58°33'40''.5$	11.77	8.32E-14	9.E-16	5.79E-14	3.E-16
Arp 299	IC 0694	$11^h28^m33^s.67$	$+58°33'46''.1$	11.41	3.59E-14	4.E-16	2.30E-14	1.E-16
ESO 440-IG058	ESO 440-IG058 NED01	$12^h06^m51^s.70$	$-31°56'46''.4$	10.54	1.63E-15	2.E-16	2.43E-15	9.E-17
ESO 440-IG058	ESO 440-IG058 NED02	$12^h06^m51^s.87$	$-31°56'59''.2$	11.37	6.34E-16	9.E-17	1.05E-15	4.E-17
SGC 1211-470	ESO 267-G029	$12^h13^m52^s.28$	$-47°16'25''.4$	11.18	5.66E-15	5.E-16	4.23E-15	9.E-16
SGC 1211-470	ESO 267-G030	$12^h14^m12^s.81$	$-47°13'42''.5$	11.23	2.29E-15	4.E-16	2.23E-15	8.E-16
NGC 4922	NGC 4922 NED01	$13^h01^m24^s.51$	$+29°18'29''.8$	8.87	3.55E-16	1.E-17	8.25E-16	6.E-18
NGC 4922	NGC 4922 NED02	$13^h01^m25^s.27$	$+29°18'49''.5$	11.38	1.04E-15	3.E-17	1.37E-15	1.E-17
MCG-02-33-098-9	MCG-02-33-098	$13^h02^m19^s.66$	$-15°46'04''.2$	11.00	1.39E-15	9.E-17	3.22E-15	7.E-17
MCG-02-33-098-9	MCG-02-33-099	$13^h02^m20^s.38$	$-15°45'59''.6$	10.66	4.11E-15	3.E-16	3.89E-15	8.E-17
VV 250	VV 250b	$13^h15^m30^s.69$	$+62°07'45''.8$	...	2.92E-15	1.E-16	2.80E-15	4.E-17
VV 250	VV 250a	$13^h15^m34^s.96$	$+62°07'29''.2$	...	5.74E-15	3.E-16	6.06E-15	1.E-16
NGC 5256	MRK 266B	$13^h38^m17^s.25$	$+48°16'32''.9$	11.37	4.38E-15	2.E-16	4.00E-15	7.E-17
NGC 5256	MRK 266A	$13^h38^m17^s.79$	$+48°16'41''.6$	11.11	5.80E-15	2.E-16	5.45E-15	9.E-17
Arp 240	NGC 5257	$13^h39^m52^s.95$	$+00°50'25''.9$	11.31	1.10E-14	4.E-16	9.63E-15	4.E-16
Arp 240	NGC 5258	$13^h39^m57^s.72$	$+00°49'53''.0$	11.32	2.84E-14	6.E-16	2.11E-14	5.E-16
NGC 5331	NGC 5331 NED01	$13^h52^m16^s.21$	$+02°06'05''.1$	11.54	1.32E-15	2.E-17	1.59E-15	6.E-18
NGC 5331	NGC 5331 NED02	$13^h52^m16^s.43$	$+02°06'30''.9$	11.02	3.89E-15	5.E-17	3.64E-15	1.E-17
GOALS J144510.0-205331	NGC 5734	$14^h45^m09^s.04$	$-20°52'13''.2$	11.04	2.64E-15	3.E-16	4.03E-15	7.E-16
GOALS J144510.0-205331	NGC 5743	$14^h45^m11^s.02$	$-20°54'48''.6$	10.86	1.06E-14	4.E-16	9.61E-15	7.E-16

Table 2
(Continued)

System Name (1)	Galaxy Name (2)	R.A. (J2000) (3)	Decl. (J2000) (4)	log(L_{IR}) (5)	f_ν(FUV) (6)	σ_{FUV} (7)	f_ν(NUV) (8)	σ_{NUV} (9)
VV 340	VV 340b	$14^h57^m00\overset{s}{.}32$	$+24°36'24\overset{''}{.}6$	10.83	3.48E-15	4.E-17	2.96E-15	1.E-17
VV 340	VV 340a	$14^h57^m00\overset{s}{.}70$	$+24°37'05\overset{''}{.}8$	11.69	1.02E-15	2.E-17	8.53E-16	6.E-18
Arp 293	NGC 6285	$16^h58^m23\overset{s}{.}99$	$+58°57'21\overset{''}{.}7$	10.72	3.80E-15	2.E-16	3.47E-15	3.E-16
Arp 293	NGC 6286	$16^h58^m31\overset{s}{.}63$	$+58°56'13\overset{''}{.}3$	11.36	3.52E-15	2.E-16	2.99E-15	3.E-16
UGC 11175	NGC 6621	$18^h12^m55\overset{s}{.}39$	$+68°21'48\overset{''}{.}2$	11.28	1.86E-15	9.E-17	2.93E-15	5.E-17
UGC 11175	NGC 6621 SE	$18^h12^m58\overset{s}{.}52$	$+68°21'29\overset{''}{.}4$	9.52	3.63E-15	2.E-16	2.73E-15	5.E-17
UGC 11175	NGC 6622	$18^h12^m59\overset{s}{.}68$	$+68°21'15\overset{''}{.}1$	9.23	1.48E-16	7.E-18	4.79E-16	9.E-18
KTS57	IC 4686	$18^h13^m38\overset{s}{.}77$	$-57°43'57\overset{''}{.}3$	11.02	1.13E-14	3.E-16	1.08E-14	1.E-16
KTS57	IC 4687	$18^h13^m39\overset{s}{.}80$	$-57°43'30\overset{''}{.}7$	11.32	4.11E-15	1.E-16	3.52E-15	4.E-17
KTS57	IC 4689	$18^h13^m40\overset{s}{.}38$	$-57°44'54\overset{''}{.}3$	11.02	1.92E-15	2.E-16	1.51E-15	4.E-16
NGC 6670AB	NGC 6670B	$18^h33^m32\overset{s}{.}78$	$+59°53'11\overset{''}{.}7$	11.32	7.77E-16	2.E-17	8.71E-16	9.E-18
NGC 6670AB	NGC 6670A	$18^h33^m37\overset{s}{.}67$	$+59°53'21\overset{''}{.}3$	11.38	1.86E-15	3.E-17	1.73E-15	1.E-17
ESO 343-IG013	ESO 343-IG013 NED01	$21^h36^m10\overset{s}{.}53$	$-38°32'42\overset{''}{.}8$	10.60	2.63E-15	2.E-16	2.76E-15	9.E-17
ESO 343-IG013	ESO 343-IG013 NED02	$21^h36^m10\overset{s}{.}93$	$-38°32'33\overset{''}{.}0$	10.99	1.32E-15	1.E-16	1.49E-15	5.E-17
Arp 298	NGC 7469	$23^h03^m15\overset{s}{.}64$	$+08°52'25\overset{''}{.}5$	11.58	4.32E-14	1.E-16	3.11E-14	1.E-16
Arp 298	IC 5283	$23^h03^m18\overset{s}{.}04$	$+08°53'36\overset{''}{.}5$	10.79	1.77E-15	3.E-17	1.76E-15	5.E-17
NGC 7592	NGC 7592A	$23^h18^m21\overset{s}{.}78$	$-04°24'57\overset{''}{.}0$	11.17	2.35E-15	6.E-17	1.66E-15	2.E-17
NGC 7592	NGC 7592B	$23^h18^m22\overset{s}{.}60$	$-04°24'58\overset{''}{.}0$	11.01	2.09E-14	5.E-16	1.21E-14	2.E-16
ESO 077-IG014	ESO 077-IG014 NED01	$23^h21^m03\overset{s}{.}73$	$-69°13'01\overset{''}{.}0$	11.33	5.08E-16	4.E-17	8.42E-16	9.E-18
ESO 077-IG014	ESO 077-IG014 NED02	$23^h21^m05\overset{s}{.}45$	$-69°12'47\overset{''}{.}3$	11.56	2.64E-17	2.E-18	1.91E-16	2.E-18
Arp 182	NGC 7674	$23^h27^m56\overset{s}{.}71$	$+08°46'44\overset{''}{.}3$	11.55	1.30E-14	1.E-16	9.96E-15	4.E-17
Arp 182	NGC 7674A	$23^h27^m58\overset{s}{.}77$	$+08°46'57\overset{''}{.}9$	10.01	1.23E-15	1.E-17	1.64E-15	6.E-18
GOALS J2341454-033944	MRK 933	$23^h41^m43\overset{s}{.}69$	$-03°39'26\overset{''}{.}5$	10.17	3.02E-15	6.E-17	2.88E-15	9.E-17
GOALS J2341454-033944	MCG-01-60-021	$23^h41^m47\overset{s}{.}33$	$-03°40'01\overset{''}{.}7$	10.43	3.58E-16	3.E-17	...	...
GOALS J2341454-033944	MCG-01-60-022	$23^h42^m00\overset{s}{.}91$	$-03°36'54\overset{''}{.}4$	11.15	7.99E-15	1.E-16	6.20E-15	2.E-16
KTG 82	NGC 7769	$23^h51^m03\overset{s}{.}91$	$+20°09'01\overset{''}{.}7$	10.74	3.39E-14	8.E-17	2.35E-14	6.E-17
KTG 82	NGC 7770	$23^h51^m22\overset{s}{.}55$	$+20°05'49\overset{''}{.}2$	10.67	1.07E-14	4.E-17	7.63E-15	3.E-17
KTG 82	NGC 7771	$23^h51^m24\overset{s}{.}80$	$+20°06'42\overset{''}{.}2$	11.17	5.13E-15	3.E-17	6.39E-15	3.E-17

Note. Column 1: system name; Column 2: galaxy name; Column 3: the right ascension (J2000) of the IRAC 8 μm centroid in J. Mazzarella et al. (2010, in preparation); Column 4: the declination (J2000) of the IRAC 8 μm centroid in J. Mazzarella et al. (2010, in preparation); Column 5: the infrared luminosity in $\log_{10}$ Solar units computed using the MIPS flux densities reported in J. Mazzarella et al. (2010, in preparation) and the luminosity distances in Armus et al. (2009); see the text for details; Column 6: *GALEX* FUV flux density in units of erg s^{-1} cm^{-2} Å^{-1}; Column 7: *GALEX* FUV flux density uncertainty; Column 8: *GALEX* NUV flux density in units of erg s^{-1} cm^{-2} Å^{-1}; Column 9: *GALEX* NUV flux density uncertainty.

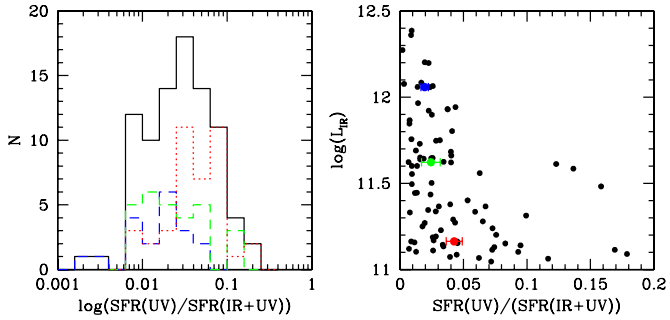

Figure 2. Left: histogram showing the ratio of SFR(UV) to SFR(UV+IR). The solid line is the full GOALS *GALEX* sample. Colored lines show the GOALS *GALEX* sample divided into luminosity bins as in Figure 1: $10^{11}\ L_\odot < L_{IR} < 10^{11.4}\ L_\odot$ (red dotted line), $10^{11.4}\ L_\odot < L_{IR} < 10^{11.8}\ L_\odot$ (green dashed line), and $L_{IR} > 10^{11.8}\ L_\odot$ (blue dashed line). The FUV contribution to SFR is small for (U)LIRGs and decreases with increasing L_{IR}. Right: L_{IR} plotted against the ratio of SFR(UV) to SFR(UV+IR). Median ratios of the star formation rates are shown for each luminosity bin (red: $10^{11}\ L_\odot < L_{IR} < 10^{11.4}\ L_\odot$, green: $10^{11.4}\ L_\odot < L_{IR} < 10^{11.8}\ L_\odot$, blue: $L_{IR} > 10^{11.8}\ L_\odot$) along with 1$\sigma$ standard deviations of the mean. Although anti-correlated (Spearman rank correlation coefficient of −0.47), the correlation is not linear.

derived from *K*-band data were used where possible. For the galaxies without reliable *K*-band photometry, the masses estimated from 3.6 μm data were scaled by the median ratio of mass(*K*)/mass(3.6) from galaxies measured at both wavelengths. Stellar masses range from 4.3×10^{10} to $6.4 \times 10^{11}\ M_\odot$, with a median of $1.4 \times 10^{11}\ M_\odot$ and a mean of $(1.63 \pm 0.09) \times 10^{11}\ M_\odot$. The specific star formation rate (SSFR; SFR per unit mass) ranges from 5.5×10^{-11} to 3.5×10^{-9} yr^{-1}, with a median of 3.9×10^{-10} yr^{-1} and a mean of $(6.2 \pm 0.7) \times 10^{-10}$ yr^{-1}. These correspond to mass doubling timescales of 18 Gyr to 290 Myr, with a median of 2.6 Gyr.

The Spitzer Infrared Nearby Galaxy Survey (SINGS; Kennicutt et al. 2003) provides a useful comparison sample of lower luminosity galaxies observed with both *GALEX* and *Spitzer*. The upper bound of the SSFRs measured for SINGS galaxies is approximately 3×10^{-10} yr^{-1} (Dale et al. 2007). The IR/UV ratio, a useful observational measure of dust extinction, is defined as

$$\mathrm{IR/UV} = \frac{L_{IR}}{\nu L_\nu(\mathrm{FUV}) + \nu L_\nu(\mathrm{NUV})} \quad (2)$$

and ranges from 5.8 to 813, with a median of 39. Figure 3 compares the IR/UV ratio against SSFR for both the GOALS and SINGS samples (Dale et al. 2007). In GOALS systems, the IR/UV ratio is correlated with SSFR ($r_s = 0.55$, significance 2×10^{-8}), with large scatter: LIRGs and ULIRGs with high SSFR also have high IR/UV ratios. The two quantities are anti-correlated ($r_s = -0.61$, significance 1×10^{-6}) for SINGS galaxies with SSFR $> 10^{-11}$ yr^{-1}. A handful of SINGS galaxies have IR/UV ratios which are as high as seen in the GOALS sample, but their SSFRs are significantly lower. Taken

Table 3
Derived Quantities—Integrated Systems

System	$\log(L_{\rm FUV})$	$\beta(GALEX)$	$\sigma_{\beta(GALEX)}$	IRX	$\sigma_{\rm IRX}$	Mass ($M_\odot$)	SFR ($M_\odot$ yr^{-1})	SSFR (yr^{-1})	IR/UV
(1)	(2)	(3)	(4)	(5)	(6)	(7)	(8)	(9)	(10)
NGC 0023	9.39	0.409	0.016	1.724	0.003	1.59E+11	23.34	1.47E-10	19.2
NGC 0034	9.69	−0.907	0.078	1.799	0.013	1.10E+11	[55.25]	[5.04E-10]	31.2
Arp 256	10.22	−0.139	0.016	1.262	0.003	1.80E+11	57.11	3.18E-10	7.6
ESO 350-IG038	10.15	−1.281	0.009	1.128	0.001	4.63E+10	[37.02]	[7.99E-10]	7.2
NGC 0232	9.04	−0.265	0.224	2.404	0.037	1.94E+11	48.65	2.50E-10	108.7
MCG+12-02-001	7.90	−1.915	2.361	3.593	0.343	8.10E+10	54.49	6.73E-10	2348.3
NGC 0317B	8.82	1.421	0.339	2.367	0.060	1.16E+11	26.97	2.33E-10	63.0
IC 1623	10.33	−0.649	0.010	1.379	0.002	1.62E+11	[94.09]	[5.80E-10]	11.2
MCG-03-04-014	9.52	0.100	0.034	2.127	0.006	1.64E+11	78.53	4.80E-10	52.5
ESO 244-G012	9.53	−0.376	0.104	1.848	0.017	1.37E+11	42.66	3.11E-10	31.1
CGCG 436-030	9.71	0.721	0.023	1.974	0.004	7.12E+10	[85.87]	[1.21E-09]	31.3
IRAS F01364-1042	8.71	2.662	0.284	3.136	0.051	4.33E+10	122.61	2.83E-09	247.6
NGC 0695	9.63	0.764	0.029	2.053	0.005	2.01E+11	84.64	4.21E-10	37.1
UGC 01385	9.50	−0.560	0.090	1.546	0.015	6.05E+10	20.32	3.36E-10	16.2
NGC 0877	9.59	−0.118	0.015	1.512	0.002	1.61E+11	22.83	1.41E-10	13.5
MCG+05-06-036	9.33	1.029	0.192	2.316	0.034	2.88E+11	77.18	2.68E-10	63.0
NGC 0958	9.62	−0.249	0.021	1.581	0.004	2.79E+11	28.71	1.03E-10	16.3
NGC 1068	9.53	−0.194	0.005	1.865	0.001	1.44E+11	[44.29]	[3.07E-10]	30.9
UGC 02238	8.74	−0.233	0.134	2.591	0.022	8.71E+10	37.70	4.33E-10	166.2
NGC 1275	9.67	−0.147	0.007	1.593	0.001	4.29E+11	[32.78]	[7.65E-11]	16.4
NGC 1365	9.24	−0.203	0.012	1.760	0.002	1.44E+11	[17.83]	[1.24E-10]	24.4
IRAS F03359+1523	8.98	0.660	0.873	2.562	0.157	5.56E+10	61.22	1.10E-09	123.2
CGCG 465-012	8.14	3.748	2.176	3.054	0.395	1.17E+11	27.51	2.35E-10	139.2
UGC 02982	8.06	−1.453	2.293	3.141	0.363	8.57E+10	27.71	3.23E-10	764.9
ESO 550-IG025	9.36	0.107	0.240	2.142	0.041	1.14E+11	56.46	4.95E-10	54.3
ESO 203-IG001	9.26	−0.195	0.112	2.606	0.019	7.33E+10	127.43	1.74E-09	170.5
MCG-05-12-006	8.69	2.091	0.388	2.479	0.069	4.39E+10	26.06	5.93E-10	65.9
CGCG 468-002	8.32	−0.940	1.609	2.900	0.269	8.37E+10	[29.15]	[3.48E-10]	396.5
IRAS 05083+2441	7.95	1.277	2.568	3.313	0.460	7.86E+10	31.95	4.06E-10	581.5
IRAS 05129+5128	8.54	0.244	1.422	2.882	0.248	5.07E+10	45.90	9.05E-10	288.1
IRAS F05189-2524	9.38	−0.362	0.130	2.783	0.022	3.19E+11	[253.48]	[7.95E-10]	266.5
NGC 1961	9.66	−0.146	0.011	1.403	0.002	3.92E+11	21.38	5.45E-11	10.6
UGC 03410	8.72	−0.199	0.218	2.383	0.037	1.23E+11	22.03	1.79E-10	102.0
NGC 2146	8.30	0.789	0.025	2.820	0.004	6.41E+10	22.87	3.57E-10	215.2
ESO 255-IG007	9.85	−0.110	0.030	2.048	0.005	1.80E+11	140.00	7.79E-10	46.1
NGC 2342	9.86	−0.274	0.063	1.453	0.011	1.97E+11	37.60	1.90E-10	12.2
NGC 2369	8.73	−0.199	0.213	2.427	0.036	1.24E+11	25.00	2.01E-10	113.0
NGC 2388	9.72	−0.721	0.015	1.559	0.002	1.43E+11	34.74	2.43E-10	17.3
MCG+02-20-003	9.45	−0.563	0.096	1.680	0.016	8.22E+10	[24.22]	[2.95E-10]	22.0
NGC 2623	9.25	−0.234	0.038	2.351	0.006	6.42E+10	69.19	1.08E-09	95.6
ESO 060-IG016	9.32	0.945	0.238	2.495	0.042	9.37E+10	[115.40]	[1.23E-09]	97.5
IRAS F08572+3915	9.62	0.791	0.103	2.548	0.018	6.38E+11	[254.32]	[3.98E-10]	115.1
IRAS 09022-3615	8.86	3.672	0.650	3.451	0.118	1.66E+11	[359.05]	[2.17E-09]	356.6
IRAS F09111-1007	9.44	1.304	0.106	2.619	0.019	1.43E+11	198.46	1.39E-09	116.8
UGC 04881	9.55	0.726	0.040	2.197	0.007	2.59E+11	97.13	3.76E-10	52.3
UGC 05101	9.09	0.876	0.136	2.925	0.024	1.97E+11	[180.18]	[9.15E-10]	267.6
MCG+08-18-013	9.78	−0.974	0.100	1.555	0.016	7.42E+10	39.55	5.33E-10	18.1
Arp 303	9.26	−0.220	0.153	1.968	0.026	1.73E+11	29.83	1.72E-10	39.5
NGC 3110	9.72	−0.183	0.085	1.646	0.014	1.32E+11	41.72	3.15E-10	18.6
ESO 374-IG032	9.39	2.969	0.054	2.394	0.010	2.89E+11	[106.13]	[3.67E-10]	40.3
IRAS F10173+0828	7.10	12.181	11.648	4.760	2.118	3.67E+10	126.32	3.44E-09	235.0
NGC 3221	9.19	0.169	0.119	1.896	0.020	1.55E+11	21.75	1.40E-10	30.3
NGC 3256	9.34	0.433	0.018	2.299	0.003	1.14E+11	76.46	6.71E-10	71.6
ESO 264-G036	7.54	8.485	12.042	3.781	2.189	2.45E+11	36.54	1.49E-10	114.3
IRAS F10565+2448	8.83	1.997	0.237	3.247	0.042	1.49E+11	209.13	1.40E-09	398.4
MCG+07-23-019	9.86	−0.804	0.111	1.761	0.020	9.36E+10	75.13	8.03E-10	28.0
CGCG 011-076	8.56	1.114	0.517	2.871	0.090	1.31E+11	46.52	3.55E-10	220.4
IRAS F11231+1456	9.23	0.897	0.240	2.413	0.041	1.84E+11	76.35	4.15E-10	81.8
NGC 3690	10.16	−0.923	0.029	1.771	0.005	1.55E+11	[150.55]	[9.74E-10]	29.4
ESO 320-G030	8.47	0.633	0.255	2.693	0.045	4.63E+10	25.64	5.54E-10	168.0
ESO 440-IG058	9.11	1.027	0.336	2.325	0.059	1.24E+11	47.53	3.83E-10	64.4
IRAS F12112+0305	9.85	−0.606	0.064	2.510	0.010	2.17E+11	402.89	1.85E-09	150.4
ESO 267-G030	8.99	−0.060	0.473	2.260	0.082	2.57E+11	31.31	1.22E-10	74.4
NGC 4922	8.89	1.073	0.080	2.489	0.014	1.73E+11	[41.95]	[2.42E-10]	92.6

Table 3
(Continued)

System	$\log(L_{\rm FUV})$	$\beta(GALEX)$	$\sigma_{\beta(GALEX)}$	IRX	$\sigma_{\rm IRX}$	Mass ($M_\odot$)	SFR ($M_\odot$ yr^{-1})	SSFR (yr^{-1})	IR/UV
(1)	(2)	(3)	(4)	(5)	(6)	(7)	(8)	(9)	(10)
CGCG 043-099	9.36	−0.516	0.299	2.330	0.048	1.19E+11	84.73	7.11E-10	97.2
MCG-02-33-098-9	9.19	0.612	0.161	1.973	0.028	5.91E+10	25.87	4.38E-10	32.2
ESO 507-G070	9.01	−0.040	0.115	2.544	0.020	1.23E+11	62.77	5.12E-10	142.1
VV 250a	9.89	0.057	0.111	1.913	0.019	1.12E+11	113.75	1.01E-09	32.4
UGC 08387	9.35	0.284	0.156	2.379	0.026	6.72E+10	94.18	1.40E-09	89.6
NGC 5104	9.05	−0.060	0.210	2.220	0.035	1.36E+11	32.52	2.38E-10	67.7
MCG-03-34-064	8.99	0.022	0.488	2.204	0.042	1.19E+11	[27.08]	[2.27E-10]	63.7
NGC 5135	9.49	0.195	0.084	1.804	0.014	1.27E+11	[35.41]	[2.79E-10]	24.4
IC 4280	9.49	0.391	0.109	1.661	0.019	1.45E+11	25.24	1.74E-10	16.7
NGC 5256	9.88	−0.176	0.107	1.679	0.018	1.66E+11	65.00	3.92E-10	20.1
Arp 240	10.32	−0.592	0.043	1.292	0.007	3.02E+11	77.47	2.57E-10	9.1
UGC 08739	9.29	−0.730	0.183	1.854	0.030	9.89E+10	24.99	2.53E-10	34.1
NGC 5331	9.75	0.011	0.029	1.911	0.005	2.66E+11	80.41	3.02E-10	32.7
Arp 84	9.08	0.398	0.118	1.993	0.021	2.11E+11	20.99	9.94E-11	35.7
CGCG 247-020	8.48	−0.627	1.038	2.911	0.167	5.54E+10	42.81	7.72E-10	380.3
NGC 5653	9.49	0.017	0.077	1.640	0.013	1.03E+11	24.24	2.36E-10	17.5
IRAS F14348-1447	9.92	−0.792	0.138	2.466	0.023	3.74E+11	428.54	1.14E-09	141.6
NGC 5734	9.34	−0.237	0.103	1.813	0.017	1.89E+11	25.25	1.33E-10	27.7
VV 340a	9.80	−0.376	0.026	1.950	0.046	3.15E+11	98.31	3.12E-10	39.3
CGCG 049-057	7.20	5.900	5.898	4.156	1.072	1.97E+10	39.16	1.99E-09	770.7
VV 705	9.86	−0.559	0.152	2.061	0.025	1.56E+11	147.81	9.48E-10	52.9
IRAS F15250+3608	9.82	−0.169	0.191	2.264	0.034	6.08E+10	211.11	3.47E-09	77.0
NGC 5936	9.69	−0.398	0.064	1.450	0.011	9.68E+10	25.23	2.61E-10	12.5
UGC 09913	8.85	0.997	0.329	3.423	0.038	1.16E+11	327.74	2.82E-09	813.3
NGC 5990	9.32	−0.190	0.106	1.817	0.018	1.42E+11	[24.19]	[1.70E-10]	27.7
NGC 6052	10.01	−0.755	0.050	1.080	0.009	4.76E+10	24.09	5.06E-10	5.8
NGC 6090	10.26	−0.176	0.017	1.325	0.003	2.24E+11	71.10	3.17E-10	8.9
IRAS F16164-0746	9.05	−0.431	0.161	2.573	0.028	7.34E+10	72.75	9.91E-10	167.0
CGCG 052-037	8.97	0.430	0.352	2.475	0.061	1.18E+11	48.75	4.13E-10	107.3
NGC 6240	9.59	0.003	0.168	2.336	0.031	3.90E+11	[148.44]	[3.81E-10]	87.1
NGC 6286	9.39	−0.298	0.114	1.976	0.019	1.64E+11	41.26	2.51E-10	41.0
IRAS F17132+5313	9.53	0.364	0.073	2.435	0.013	1.72E+11	159.67	9.28E-10	99.8
IRAS F17207-0014	7.31	4.576	8.665	5.154	1.574	1.52E+11	501.22	3.29E-09	12840.8
UGC 11041	9.11	−0.559	0.174	2.000	0.029	7.92E+10	22.85	2.89E-10	45.9
CGCG 141-034	8.60	−1.561	0.773	2.597	0.117	5.60E+10	27.39	4.89E-10	222.8
NGC 6621	9.36	0.203	0.126	1.930	0.021	1.55E+11	34.28	2.21E-10	32.5
IC 4687	9.73	−0.465	0.065	1.895	0.011	1.60E+11	74.70	4.66E-10	35.3
NGC 6670AB	9.36	0.177	0.049	2.290	0.008	1.90E+11	78.26	4.12E-10	74.9
IC 4734	9.30	−0.696	0.141	2.045	0.023	9.10E+10	39.30	4.32E-10	52.6
ESO 593-IG008	9.72	1.894	0.439	2.209	0.080	3.53E+11	150.38	4.26E-10	42.9
IRAS F19297-0406	8.05	0.433	1.073	4.401	0.179	1.72E+11	494.79	2.88E-09	9041.1
ESO 339-G011	8.88	0.764	0.380	2.322	0.066	1.03E+11	[27.62]	[2.69E-10]	68.9
NGC 6907	9.98	−0.622	0.009	1.134	0.001	1.54E+11	25.24	1.64E-10	6.3
NGC 6926	9.71	−0.757	0.090	1.609	0.015	1.95E+11	[37.50]	[1.92E-10]	19.5
CGCG 448-020	10.28	−1.134	0.099	1.662	0.016	1.34E+11	156.77	1.17E-09	23.9
ESO 286-IG019	9.95	−0.206	0.027	2.108	0.005	1.13E+11	203.56	1.80E-09	54.3
ESO 286-G035	9.09	0.196	0.176	2.102	0.030	5.84E+10	27.58	4.72E-10	48.4
ESO 343-IG013	9.12	0.173	0.214	2.014	0.036	6.75E+10	24.22	3.59E-10	39.8
NGC 7130	9.71	0.327	0.017	1.712	0.003	1.45E+11	[46.88]	[3.23E-10]	19.1
IC 5179	9.62	−0.137	0.058	1.619	0.010	1.23E+11	31.01	2.52E-10	17.3
ESO 602-G025	9.30	−0.169	0.264	2.037	0.044	1.37E+11	38.38	2.80E-10	45.6
UGC 12150	7.59	5.341	5.742	3.760	1.043	1.10E+11	38.87	3.55E-10	386.2
IRAS F22491-1808	10.00	0.176	0.076	2.198	0.013	2.27E+11	279.16	1.23E-09	60.7
NGC 7469	10.02	−0.748	0.008	1.632	0.001	2.39E+11	[80.26]	[3.35E-10]	20.6
CGCG 453-062	8.61	1.285	0.659	2.768	0.116	8.99E+10	41.52	4.62E-10	165.3
ESO 148-IG002	10.01	−0.282	0.025	2.054	0.004	1.06E+11	204.60	1.94E-09	48.8
IC 5298	9.15	−0.553	0.312	2.451	0.051	1.29E+11	69.67	5.38E-10	129.7
NGC 7552	9.32	0.403	0.005	1.793	0.001	7.62E+10	[22.98]	[3.01E-10]	22.5
NGC 7592	10.07	−1.240	0.067	1.332	0.011	1.13E+11	[47.03]	[4.15E-10]	11.4
ESO 077-IG014	8.90	1.576	0.211	2.856	0.038	1.77E+11	100.48	5.68E-10	185.3
NGC 7674	10.00	−0.489	0.022	1.560	0.004	3.03E+11	[65.76]	[2.17E-10]	16.4
IRAS F23365+3604	9.33	3.515	0.183	2.872	0.033	1.41E+11	276.72	1.96E-09	99.8
MCG-01-60-022	9.52	−0.671	0.031	1.752	0.005	2.08E+11	33.35	1.61E-10	26.6
Arp 86	9.40	−0.263	0.030	1.667	0.005	2.84E+11	21.21	7.47E-11	19.9

Table 3
(Continued)

System	$\log(L_{\rm FUV})$	$\beta(GALEX)$	$\sigma_{\beta(GALEX)}$	IRX	$\sigma_{\rm IRX}$	Mass ($M_\odot$)	SFR ($M_\odot$ yr^{-1})	SSFR (yr^{-1})	IR/UV
(1)	(2)	(3)	(4)	(5)	(6)	(7)	(8)	(9)	(10)
NGC 7771	9.78	−0.880	0.006	1.621	0.001	4.00E+11	45.12	1.13E-10	20.6
MRK0331	8.92	0.129	0.094	2.575	0.016	8.23E+10	55.14	6.70E-10	146.4

Notes. Column 1: system name; Column 2: the total FUV luminosity in $\log_{10}$ Solar units; Column 3: $\beta(GALEX)$ calculated as described in Section 3.1, Equation (1); Column 4: $\beta(GALEX)$ uncertainty; Column 5: ratio of IR to FUV flux IRX calculated as described in Section 3.1; Column 6: IRX uncertainty; Column 7: stellar mass calculated as described in Section 3.2; Column 8: star formation rate calculated as described in Section 3.2. Values in brackets should be considered upper limits due to possible AGN contamination. Column 9: specific star formation rate calculated as described in Section 3.2. Values in brackets should be considered upper limits due to possible AGN contamination. Column 10: IR/UV ratio calculated as described in Section 3.2, Equation (2).

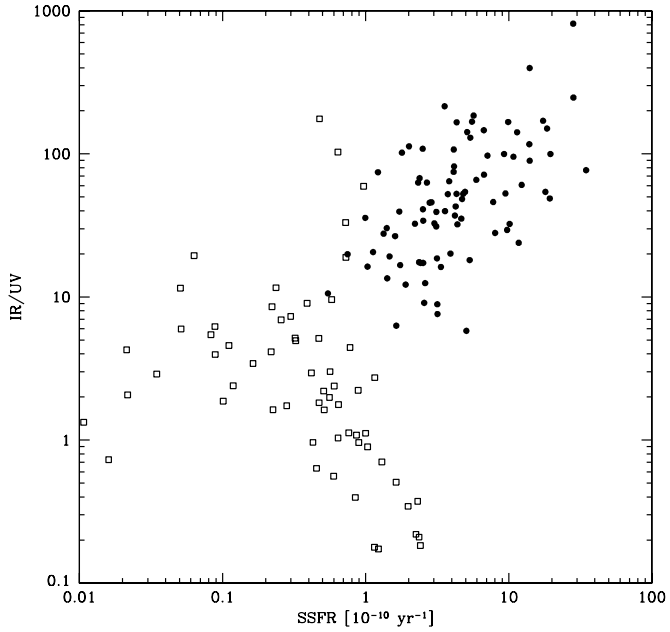

Figure 3. IR/UV ratio plotted against specific star formation rate. Solid circles are GOALS galaxies (not including those with IRAC colors suggesting a strong AGN), while open squares are SINGS galaxies (Dale et al. 2007). The GOALS outlier at the high IR/UV, high SSFR extreme is Arp 220. LIRGs and ULIRGs have much higher IR/UV ratios and SSFR than lower luminosity galaxies, and the two quantities are correlated for GOALS systems and anti-correlated for SINGS galaxies with SSFR $> 10^{-11}$ yr^{-1}.

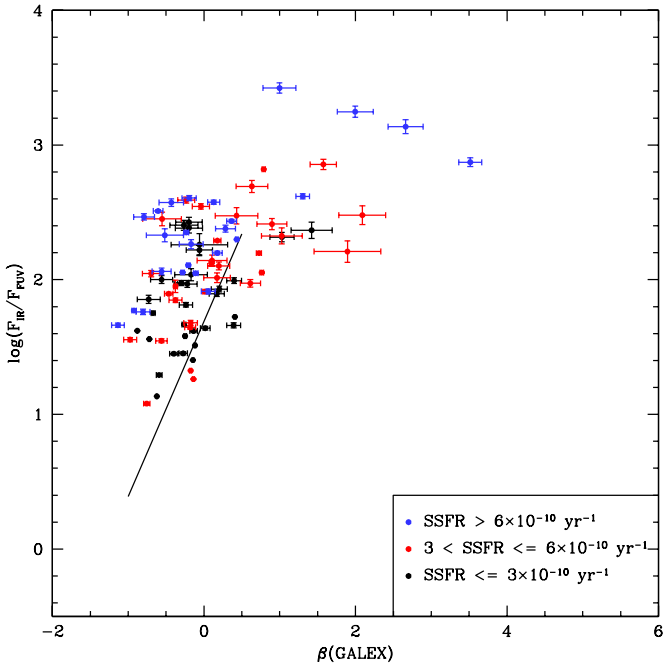

Figure 4. IRX–$\beta(GALEX)$ plot with GOALS systems (not including those with IRAC colors suggesting a strong AGN) color coded by specific SFR: black points have SSFR within the range spanned by SINGS galaxies, red points have up to twice the SSFR of any SINGS galaxy, and blue points have more than twice the SSFR of any SINGS galaxy. The solid line is the same as in Figure 1. Systems with higher SSFR are systematically redder in β and have larger IRX than systems with lower SSFR.

together, the GOALS and SINGS sources span nearly 4 orders of magnitude in IR/UV at high SSFR ($>10^{-10}$ yr^{-1}), probing very different star-forming populations.

To investigate subpopulations of the GOALS sample in SSFR, we define bins with SSFR $< 3 \times 10^{-10}$ yr^{-1}, $3 \times 10^{-10} <$ SSFR $< 6 \times 10^{-10}$ yr^{-1}, and SSFR $> 6 \times 10^{-10}$ yr^{-1}: galaxies which span the same range of SSFR as the SINGS sample, galaxies with up to twice the SSFR as the most extreme SINGS galaxies, and galaxies with more than twice the SSFR of the most extreme SINGS galaxies, respectively. These subpopulations are plotted on the IRX–$\beta(GALEX)$ diagram in Figure 4. The systems with higher SSFR have higher median offsets from the starburst relation than systems with lower SSFR. Median β values are -0.2 ± 0.2, 0.1 ± 0.1, and -0.20 ± 0.09 (high, medium, and low SSFR bins, respectively). Median IRX values are 2.35 ± 0.09, 2.10 ± 0.08, and 1.81 ± 0.06, respectively. Systems with $\beta < 0.5$ allowing a direct comparison to the starburst relation have median vertical deviations of 0.9 ± 0.1, 0.4 ± 0.1, and 0.37 ± 0.09, respectively.

3.3. Resolved Systems

A number of the interacting LIRGs in GOALS are near enough to resolve with both *GALEX* and *Spitzer* and derive IR and UV properties for each galaxy. Derived quantities for the galaxies in resolved systems are presented in Table 4. The component galaxies of resolved pair/triple systems are plotted on the IRX–$\beta(GALEX)$ diagram in Figure 5. Many GOALS systems consist of an LIRG with one or more sub-LIRG companions. The sub-LIRG galaxies are on average consistent with the GDP sample. LIRGs are on average offset above the starburst relation, with $L_{\rm IR} > 10^{11.4}$ $L_\odot$ systems having larger offsets than lower luminosity LIRGs. For systems with $\beta < 0.5$, median offsets are 1.1 ± 0.2 and 0.4 ± 0.1 for the $L_{\rm IR} > 10^{11.4}$ $L_\odot$ and 10^{11} $L_\odot < L_{\rm IR} < 10^{11.4}$ $L_\odot$ populations, respectively. An individual galaxy in general does not lie in the same region of the IRX–β diagram as the LIRG system of which it is a component; see Section 4.3 for further discussion.

Of the 18 resolved systems for which masses could be estimated, the median mass ratio of the galaxy companions is

Table 4
Derived Quantities—Resolved Components

Galaxy	$\log(L_{\rm FUV})$	$\beta(GALEX)$	$\sigma_{\beta(GALEX)}$	IRX	$\sigma_{\rm IRX}$	Mass ($M_\odot$)	SFR ($M_\odot$ yr^{-1})	SSFR (yr^{-1})
(1)	(2)	(3)	(4)	(5)	(6)	(7)	(8)	(9)
NGC 0034	9.69	−0.91	0.15	1.739	0.013	8.92E+10	[46.91]	[5.26E-10]
NGC 0035	9.35	0.53	0.19	1.257	0.020	2.05E+10	6.99	3.41E-10
MCG-02-01-052	9.89	−0.39	0.03	0.468	0.004	...	3.95	...
MCG-02-01-051	9.95	−0.64	0.03	1.501	0.003	...	48.63	...
NGC 0232	9.04	−0.26	0.55	2.312	0.037	1.10E+11	39.14	3.57E-10
NGC 0235A	8.73	−0.18	1.05	1.998	0.062	8.46E+10	[9.21]	[1.09E-10]
NGC 0317A	7.84	4.09	0.34	1.120	0.060	8.15E+10	0.16	1.95E-12
NGC 0317B	8.77	0.76	0.34	2.412	0.060	3.44E+10	26.63	7.73E-10
IC 1623A	10.31	−0.71	0.01	0.773	0.002	1.37E+11	21.07	1.54E-10
IC 1623B	8.88	0.65	0.01	2.703	0.002	4.72E+10	[67.19]	[1.42E-09]
ESO 244-G012 NED01	9.45	−0.62	0.10	0.042	0.017	...	0.53	...
ESO 244-G012 NED02	8.79	0.49	0.10	2.584	0.017	...	41.19	...
UGC 01385	8.75	−0.28	0.48	2.271	0.040	4.74E+10	18.30	3.86E-10
KUG 0152+366	9.42	−0.62	0.16	0.399	0.016	1.31E+10	1.14	8.71E-11
NGC 0876	9.59	−0.12	0.02	0.923	0.002	2.43E+10	5.60	2.31E-10
NGC 0877	8.24	0.06	0.32	2.727	0.021	1.37E+11	16.17	1.18E-10
MCG+05-06-035	9.17	1.09	0.19	1.980	0.034	1.89E+11	24.84	1.31E-10
MCG+05-06-036	8.80	0.88	0.19	2.672	0.034	9.86E+10	51.76	5.25E-10
UGC 02894	8.80	−0.34	1.31	1.827	0.093	4.73E+10	7.28	1.54E-10
CGCG 465-012	8.15	3.75	2.38	2.920	0.395	6.95E+10	20.18	2.90E-10
ESO 550-IG025 NED01	9.28	−0.01	0.24	1.994	0.041	...	32.28	...
ESO 550-IG025 NED02	8.64	0.55	0.24	2.497	0.041	...	23.54	...
CGCG 468-002 NED01	7.07	4.40	1.61	3.669	0.269	6.54E+10	9.57	1.46E-10
CGCG 468-002 NED02	8.30	−2.57	1.61	2.751	0.269	1.83E+10	[19.52]	[1.06E-09]
IRAS 05083+2441	7.95	1.10	3.94	3.264	0.462	5.56E+10	28.38	5.11E-10
2MASX J05112888+2445593	5.66	7.79	483.06	4.650	87.595	2.30E+10	3.54	1.54E-10
UGC 03405	8.72	−0.20	0.46	1.626	0.037	3.73E+10	3.83	1.03E-10
UGC 03410	8.23	0.19	1.18	2.787	0.096	8.55E+10	18.05	2.11E-10
NGC 2341	9.15	0.80	0.31	1.830	0.032	7.10E+10	16.69	2.35E-10
NGC 2342	9.86	−0.27	0.11	1.178	0.011	1.27E+11	18.93	1.50E-10
NGC 2385	7.76	4.19	0.48	1.923	0.079	2.76E+10	0.84	3.04E-11
NGC 2388	9.72	−0.72	0.03	1.453	0.002	7.73E+10	26.11	3.38E-10
NGC 2389	7.11	3.86	2.12	3.453	0.334	3.83E+10	6.34	1.65E-10
NGC 2416	9.45	−0.56	0.20	...	...	3.30E+10	...	...
MCG+02-20-003	9.14	0.73	0.25	...	...	4.92E+10	...	...
2MASX J09133644-1019296	7.90	2.62	1.02	4.049	0.181	...	154.77	...
2MASX J09133888-1019196	9.45	1.10	0.06	1.942	0.010	...	42.94	...
UGC 04881 NED02	7.98	0.82	0.22	3.285	0.038	8.52E+10	32.23	3.78E-10
UGC 04881 NED01	8.37	0.78	0.13	3.192	0.023	1.73E+11	63.94	3.69E-10
CGCG 239-011 NED01	9.63	−1.39	0.23	0.345	0.020	6.25E+09	1.65	2.64E-10
MCG+08-18-013	9.25	−0.19	0.32	2.066	0.032	6.79E+10	36.24	5.34E-10
2MASX J11210825-0259399	8.26	−0.51	2.74	2.127	0.154	9.64E+09	4.23	4.39E-10
CGCG 011-076	8.25	2.09	1.27	3.134	0.157	1.21E+11	42.19	3.48E-10
IC 2810A	9.19	0.93	0.40	2.266	0.044	1.21E+11	49.68	4.09E-10
IC 2810B	8.14	0.56	3.82	3.035	0.253	6.26E+10	26.21	4.19E-10
NGC 3690	10.00	−0.87	0.03	1.766	0.005	1.26E+11	[101.44]	[8.02E-10]
IC 0694	9.63	−1.06	0.03	1.780	0.005	7.79E+10	[45.19]	[5.80E-10]
ESO 440-IG058 NED01	8.97	0.95	0.34	1.574	0.059	...	6.02	...
ESO 440-IG058 NED02	8.56	1.20	0.34	2.819	0.059	...	41.15	...
ESO 267-G029	9.39	−0.70	0.52	1.537	0.037	9.56E+10	14.52	1.52E-10
ESO 267-G030	8.99	−0.06	1.00	1.986	0.082	1.61E+11	16.52	1.03E-10
NGC 4922 NED01	8.30	2.02	0.08	0.576	0.014	...	0.13	...
NGC 4922 NED02	8.76	0.64	0.08	2.615	0.014	...	[41.61]	...
MCG-02-33-098	8.60	2.00	0.16	2.406	0.028	...	17.52	...
MCG-02-33-099	9.07	−0.13	0.16	1.593	0.028	...	7.93	...
VV 250b	9.42	−0.10	0.11	...	...	4.60E+10	...	...
VV 250a	9.72	0.13	0.11	...	...	6.62E+10	...	...
MRK 266B	9.51	−0.22	0.11	1.853	0.018	...	40.44	...
MRK 266A	9.64	−0.15	0.11	1.477	0.018	...	22.48	...
NGC 5257	9.77	−0.33	0.13	1.541	0.014	1.42E+11	35.66	2.50E-10
NGC 5258	10.18	−0.70	0.08	1.136	0.009	1.59E+11	36.03	2.26E-10
NGC 5331 NED01	9.15	0.45	0.03	2.393	0.005	...	60.78	...
NGC 5331 NED02	9.62	−0.16	0.03	1.398	0.005	...	18.10	...
NGC 5734	8.73	1.01	0.48	2.204	0.051	1.23E+11	15.09	1.23E-10

Table 4
(Continued)

Galaxy	$\log(L_{\rm FUV})$	$\beta(GALEX)$	$\sigma_{\beta(GALEX)}$	IRX	$\sigma_{\rm IRX}$	Mass ($M_\odot$)	SFR ($M_\odot$ yr^{-1})	SSFR (yr^{-1})
(1)	(2)	(3)	(4)	(5)	(6)	(7)	(8)	(9)
NGC 5743	9.34	−0.24	0.20	1.401	0.017	6.63E+10	9.56	1.44E-10
VV 340b	9.58	−0.39	0.03	1.425	0.005	6.86E+10	17.56	2.56E-10
VV 340a	9.05	−0.44	0.06	2.610	0.010	2.46E+11	79.04	3.21E-10
NGC 6285	9.11	−0.22	0.25	1.532	0.026	3.84E+10	7.58	1.97E-10
NGC 6286	9.07	−0.39	0.28	2.204	0.027	1.26E+11	33.01	2.63E-10
NGC 6621	8.87	1.09	0.13	2.401	0.021	...	32.78	...
NGC 6621 SE	9.17	−0.69	0.13	0.355	0.021	...	0.58	...
NGC 6622	7.78	2.81	0.13	1.451	0.021	...	0.29	...
IC 4686	9.54	−0.12	0.07	1.499	0.012	2.28E+10	19.22	8.41E-10
IC 4687	9.10	−0.38	0.07	2.241	0.012	8.69E+10	38.51	4.43E-10
IC 4689	8.77	−0.57	0.62	2.176	0.045	5.04E+10	15.49	3.07E-10
NGC 6670B	8.77	0.27	0.08	2.558	0.014	1.25E+11	36.78	2.95E-10
NGC 6670A	9.14	−0.17	0.05	2.229	0.008	6.53E+10	41.39	6.34E-10
ESO 343-IG013 NED01	8.95	0.12	0.21	1.649	0.036	...	6.85	...
ESO 343-IG013 NED02	8.65	0.28	0.21	2.342	0.036	...	17.01	...
NGC 7469	10.00	−0.78	0.01	1.585	0.001	1.95E+11	[66.69]	[3.41E-10]
IC 5283	8.61	−0.02	0.08	2.179	0.007	4.39E+10	10.72	2.44E-10
NGC 7592A	9.08	−0.83	0.07	2.097	0.011	...	[25.85]	...
NGC 7592B	10.02	−1.29	0.07	0.991	0.011	...	17.96	...
ESO 077-IG014 NED01	8.88	1.21	0.21	2.448	0.038	1.23E+11	37.28	3.04E-10
ESO 077-IG014 NED02	7.60	4.73	0.21	3.960	0.038	5.42E+10	62.98	1.16E-09
NGC 7674	9.96	−0.64	0.02	1.587	0.004	2.49E+11	[61.26]	[2.46E-10]
NGC 7674A	8.94	0.69	0.02	1.072	0.004	5.37E+10	1.77	3.29E-11
MRK 933	9.14	−0.11	0.09	0.772	0.008	6.43E+09	1.41	2.19E-10
MCG-01-60-021	8.21	...	...	1.963	0.035	1.30E+11	2.59	2.00E-11
MCG-01-60-022	9.56	−0.61	0.07	1.654	0.005	7.16E+10	28.44	3.97E-10
NGC 7769	9.78	−0.88	0.01	0.961	0.001	1.38E+11	9.53	6.90E-11
NGC 7770	9.28	−0.80	0.01	1.396	0.002	2.59E+10	[8.16]	[3.15E-10]
NGC 7771	8.96	0.52	0.02	2.214	0.003	2.37E+11	25.79	1.09E-10

Notes. Column 1: galaxy name; Column 2: the total FUV luminosity in $\log_{10}$ Solar units; Column 3: $\beta(GALEX)$ calculated as described in Section 3.1, Equation (1); Column 4: $\beta(GALEX)$ uncertainty; Column 5: ratio of IR to FUV flux IRX calculated as described in Section 3.1; Column 6: IRX uncertainty; Column 7: stellar mass calculated as described in Section 3.2; Column 8: star formation rate calculated as described in Section 3.2. Values in brackets should be considered upper limits due to possible AGN contamination. Column 9: specific star formation rate calculated as described in Section 3.2. Values in brackets should be considered upper limits due to possible AGN contamination.

2.6:1, with a range from 1.1:1 to 8.1:1. The high mass component of these pairs/triples is, on average, offset above the starburst relation (Figure 6), while the low mass components are, on average, consistent with the starburst relation. For systems with $\beta < 0.5$, median offsets are 0.9 ± 0.1 and 0.3 ± 0.1 for the high mass and low mass components, respectively.

4. DISCUSSION

The complete sample of the nearest LIRGs and ULIRGs that comprise GOALS is ideal for studying the relationship between the IR and UV properties of LIRGs. A key diagnostic tool which we explore in this paper is the IRX–$\beta(GALEX)$ diagram, comparing the IR excess (ratio of IR to FUV emission) to the FUV–NUV color parameterized as the power-law slope $\beta(GALEX)$. If a class of galaxies, such as starburst galaxies, follows tight relations on this diagram, then the measurement of the rest-frame UV color allows IRX and thus $L_{\rm IR}$ to be derived. This is of particular interest at high redshift, where $L_{\rm IR}$ can only be directly measured using far-infrared and submillimeter observations but rest-frame UV observations can be made at visual wavelengths in deep surveys. Since LIRGs contribute significantly to the star formation activity at high redshift (e.g., Magnelli et al. 2009), understanding the IRX–$\beta(GALEX)$ relation in this population is extremely important. The IRX–$\beta(GALEX)$ diagram, and the combination of UV and IR data more generally, provides an indication of the obscuration to the young stars (or active nucleus) within a galaxy. This can provide a rough test of the evolutionary sequence in which some starburst galaxies transition from LIRGs to ULIRGs to QSO hosts over the course of a major merger event as the dust and gas is first funneled toward the nuclei fueling a starburst, only to be cleared away by the action of AGN and starburst winds in the final stages of the transformation to a QSO.

To estimate the importance of high-β galaxies among the IR population as a whole, the fraction of the total IR luminosity integrated over all 629 galaxies in the RBGS contributed by the 112 LIRGs and ULIRGs of the GOALS *GALEX* sample is shown as a function of β in Figure 7. Within the GOALS sample, more luminous systems have, on average, larger IRX and redder β values than less luminous systems while maintaining roughly the same offset from the starburst relation. As shown in Figure 7, a minimum of 19% of the total infrared luminosity of the 629 galaxies that comprise the RBGS is produced in LIRGs and ULIRGs with a $\beta > 0$ (*IUE* or *GALEX*). These red sources are typically absent from UV-selected samples at high redshift,

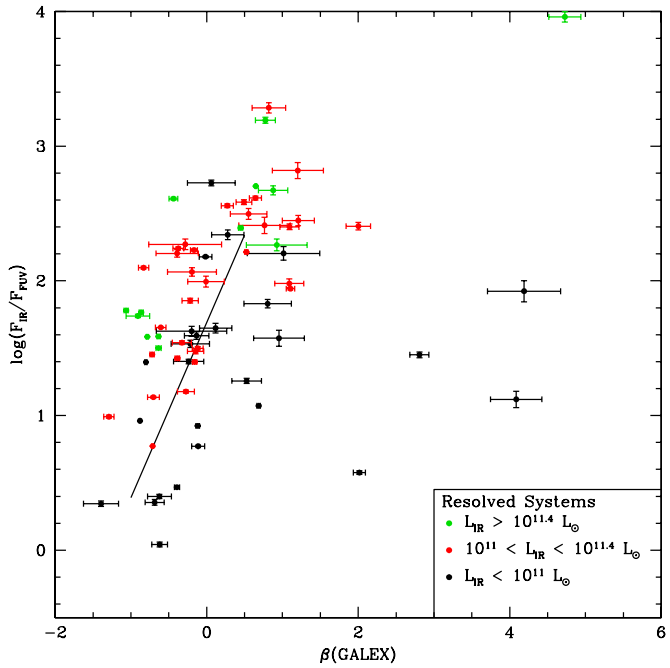

Figure 5. IRX–β(*GALEX*) plot showing the locations of individual galaxies in resolved pairs. As in Figure 1, black points have $L_{\rm IR} < 10^{11}$ $L_{\odot}$, red points have 10^{11} $L_{\odot} < L_{\rm IR} < 10^{11.4}$ $L_{\odot}$, and green points have $10^{11.4}$ $L_{\odot} < L_{\rm IR} < 10^{11.8}$ $L_{\odot}$. The solid line is the same as in Figure 1. Sub-LIRG galaxies are on average consistent with the GDP sample. LIRGs are on average offset above the starburst relation, with $L_{\rm IR} > 10^{11.4}$ $L_{\odot}$ systems having larger offsets than lower luminosity LIRGs.

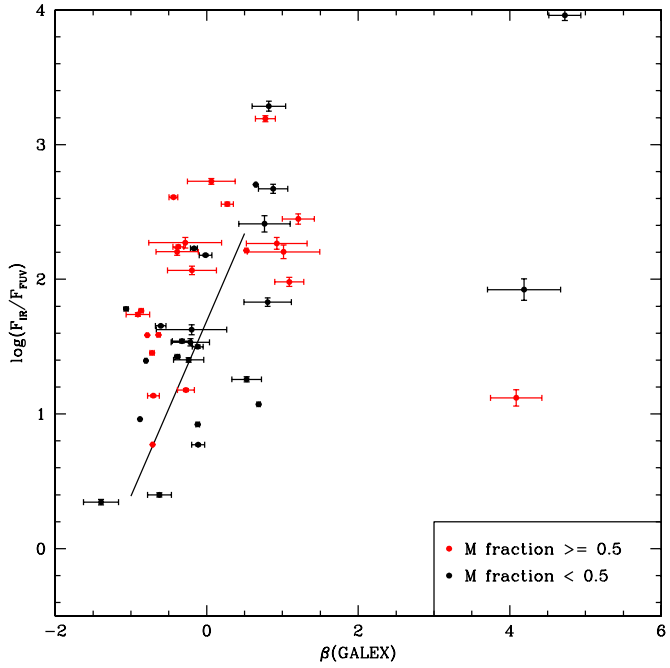

Figure 6. IRX–β(*GALEX*) plot showing the location of individual galaxies in close pairs for which a mass could be estimated. The galaxy with >50% of the mass in each system is shown in red, while other galaxies are in black. The solid line shows the starburst relation, as in Figure 1. On average, the high mass galaxy in a system is offset above the starburst relation, while the lower mass galaxy lies slightly below the starburst relation.

regardless of their estimated IR luminosity. This is a strict lower limit, since there are a number of low-z LIRGs not observed or detected with *GALEX* which might have large β.

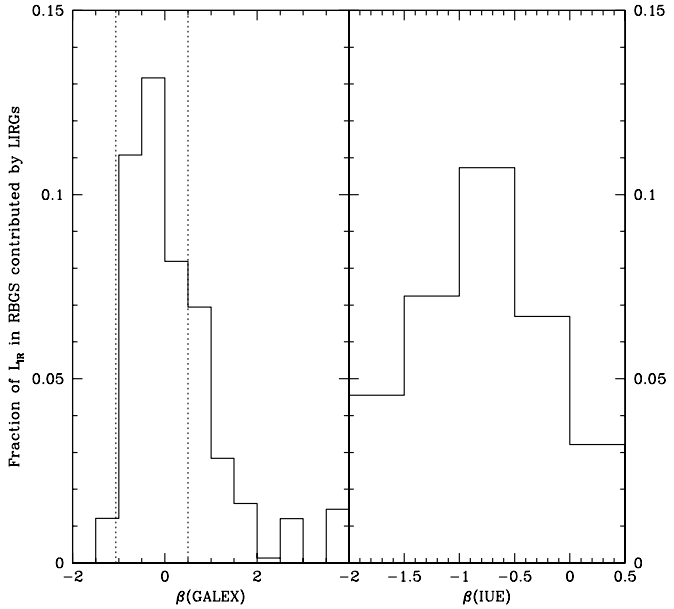

Figure 7. Fraction of total IR luminosity summed over all 629 systems in the RBGS sample contributed by LIRGs and ULIRGs with known UV colors (the GOALS *GALEX* sample, 112 systems). The IR luminosity fraction defined in this way is shown as a function of β(*GALEX*) (left panel) and β(*IUE*) (right panel) over the range of the conversion given in the Appendix. The dotted lines in the left panel mark the range of β(*GALEX*) shown in the right panel. At least 19% of the IR luminosity of the RBGS is produced by (U)LIRGs with red UV colors ($\beta > 0$).

4.1. Explaining Scatter in the IRX–β(GALEX) Relation

The trend for certain populations to have, on average, larger values of IRX and redder values of β(*GALEX*) (parallel to the starburst relation) has been explained as a sequence in optical depth (Charlot & Fall 2000). Thus, on average, more luminous LIRGs and ULIRGs have more extinction than less luminous LIRGs, and interacting systems have more extinction than non-interacting systems. This is consistent with the evolutionary scenario mentioned earlier.

We interpret the scatter of LIRGs and ULIRGs in the IRX–β(*GALEX*) diagram as follows. Deviations to the right of the starburst relation are interpreted as purely the result of redder UV colors (extra NUV emission for a given amount of FUV emission), most likely due to light from older stellar populations (Kong et al. 2004). Deviations above the starburst relation are interpreted as the result of increases in IRX, which we define as ΔIRX. This quantity is a measure of the extent to which the IR and UV emission become decoupled, for example, in heavily obscured nuclei which emit strongly in the FIR (UV radiation reprocessed by dust) but do not contribute to the observed (escaping) UV emission. Like the starburst relation, ΔIRX is not necessarily accurate for $\beta(GALEX) < -1$ or $\beta(GALEX) > 0.5$. A minimum of 11% of the total $L_{\rm IR}$ of the RBGS sample is produced in LIRGs and ULIRGs with ΔIRX > 1, an order of magnitude above the starburst relation.

Cortese et al. (2006) concluded that attempting to estimate $L_{\rm IR}$ from rest-frame UV data of high-redshift galaxies will be uncertain by >50% for normal galaxies. We find that using the starburst relation to estimate $L_{\rm IR}$ from rest-frame UV observations of LIRGs and ULIRGs would on average underestimate $L_{\rm IR}$ by a factor of 2.7 with a range of $L_{\rm IR}$(true)/$L_{\rm IR}$(estimated) between 0.2 and 68. Overestimates can be much greater for red UV colors beyond the range of the starburst

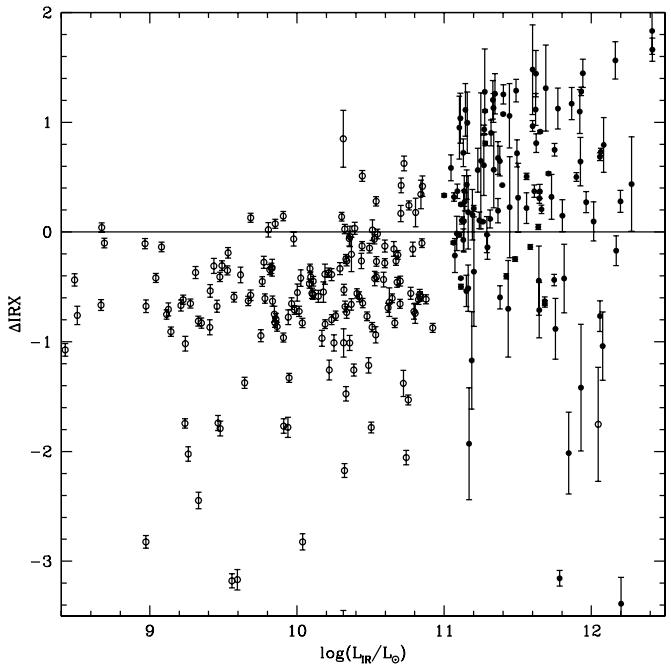

Figure 8. ΔIRX vs. $L_{\rm IR}$. GOALS systems are shown as solid points, while galaxies from GDP are shown as open points. ΔIRX increases with IR luminosity for $L_{\rm IR} \gtrsim 10^{10}\ L_{\odot}$.

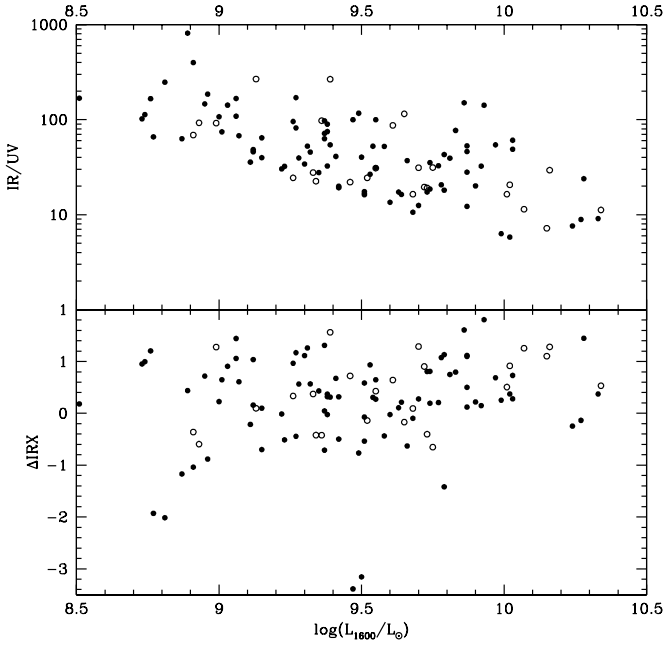

Figure 9. Top: the IR/UV ratio plotted against L_{1600}, the luminosity at 1600 Å (interpolated from FUV and NUV). The lower envelope shows the sample selection cutoff of $L_{\rm IR} > 10^{11}\ L_{\odot}$. Bottom: ΔIRX vs. L_{1600}. No trend is seen; galaxies of high ΔIRX span the full range of UV luminosity. In both panels, galaxies with IRAC colors suggesting a significant AGN contribution are shown as open circles.

relation ($\beta(GALEX) > 0.5$), up to a factor of 2400 for a linear extrapolation. Previous studies have investigated possible second parameters for the scatter of normal galaxies to the right the starburst relation. Using a sample of a wide variety of galaxy types, Seibert et al. (2005) found no correlation between the deviation from the starburst relation and $L_{\rm IR}$, $L_{\rm UV}$, $L_{\rm bol}$, or UV and optical colors. Among normal galaxies, any correlation with star formation history is weak (Kong et al. 2004; Cortese et al. 2006) or nonexistent (Seibert et al. 2005; Boquien et al. 2009).

A number of observables might explain the scatter in ΔIRX, providing a second parameter to allow more accurate measurements of $L_{\rm IR}$ at high redshift as well as physical insight into the evolution of LIRGs and ULIRGs. A central question is what mechanism(s) lead to the UV emission being heavily obscured or decoupled from the IR emission in (U)LIRGs (Goldader et al. 2002) but not in lower luminosity starbursts? Since many LIRGs and essentially all ULIRGs are merger remnants with intense, compact, dust-enshrouded nuclear starbursts or AGN, a concentration parameter might correlate with IRX–β(*GALEX*) scatter as an indicator of decoupled IR and UV emission. Similarly, warm IR colors such as *IRAS* 25 μm/60 μm might indicate dust in close proximity to a powerful UV source (starburst or AGN). AGNs provide another possible mechanism to explain scatter from the starburst relation. The [3.6]–[4.5] and [5.8]–[8] IRAC colors (Stern et al. 2005) can be used as an indicator of AGN emission. Systems identified as potential AGN might correlate with larger IRX above what the starburst relation would predict. Finally, although heightened IRX in a population of LIRGs and ULIRGs is most logically explained by elevated IR emission, it is possible for low UV emission to produce the same result.

As shown in Figure 8, ΔIRX increases with IR luminosity for $L_{\rm IR} \gtrsim 10^{10}\ L_{\odot}$, with considerable scatter. GOALS systems with IRAC colors that may indicate the presence of an AGN tend to have larger IRX ratios by a factor of 6. No correlation is found between ΔIRX and any of the following quantities: *IRAS* 25 μm/60 μm color, *IRAS* 60 μm/100 μm color, *Spitzer* 8 μm/24 μm color, $L_{\rm FUV}$, 8 μm concentration (1 kpc/total). The lack of correlation between ΔIRX and global parameters other than $L_{\rm IR}$ suggests that the decoupling between UV and IR emission takes place on sub-kpc scales in most LIRGs and ULIRGs, well below our resolution with *GALEX* and *Spitzer* MIPS 24 μm, which is 2.6 kpc (6″) at the median distance of the GOALS sample (89 Mpc). Future studies (e.g., with *Herschel* and *Hubble Space Telescope* (*HST*)) at higher spatial resolution in the FIR and UV will be able to investigate this further. Such studies have already been done for a few nearby quiescent star-forming galaxies. Boquien et al. (2009) found that variation in dust extinction curves and geometry is the most important factor determining the location of individual star-forming regions on the IRX–β diagram. Muñoz-Mateos et al. (2009) examined radial profiles of all available SINGS galaxies and found that star formation history is the primary driver determining the position on the IRX–β diagram of a radial annulus within a galaxy. The lack of correlation between ΔIRX and FIR colors suggests that when dust is close to the heating source (producing warm FIR colors), that source is obscured and the UV color β(*GALEX*) increases along with IRX. Galaxies with positive ΔIRX span a range of log($L_{\rm FUV}$) from 8.6 to 10.3 uniformly. The range of FUV luminosities indicates that LIRGs and ULIRGs with large ΔIRX value are IR bright, not UV faint. Figure 9 shows the IR/UV ratio and ΔIRX plotted against the 1600 Å luminosity (derived by linear interpolation between FUV and NUV).

In order to explore the dependence of IRX and β on the morphological properties of LIRGs, all GOALS systems were visually classified as either interacting or non-interacting based on the inspection of the *Spitzer* IRAC 3.6 μm images. A galaxy was deemed interacting if it exhibited a tidal bridge or tail, double nuclei, multiple galaxies in a common envelope, or a disturbed morphology. The interacting and non-interacting

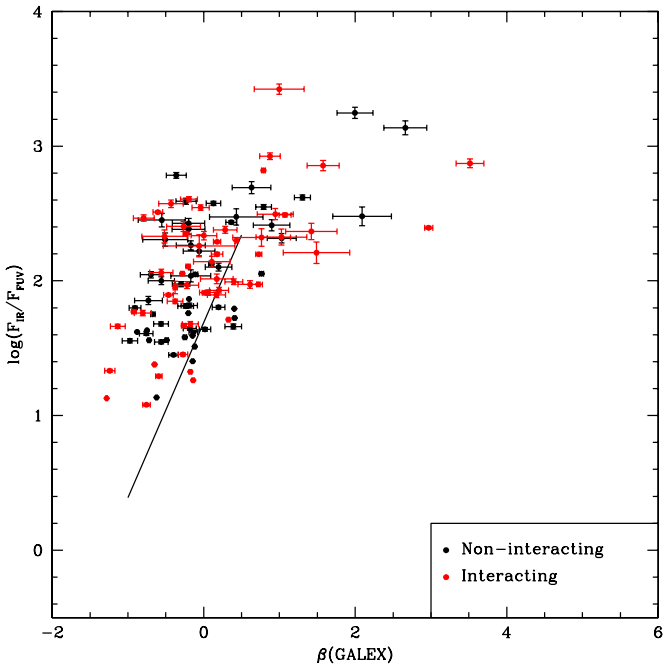

Figure 10. IRX–β(*GALEX*) plot comparing interacting (red) and non-interacting (black) LIRG systems. The solid line is the same as in Figure 1. The interacting and non-interacting populations are consistent with being drawn from the same distribution.

subpopulations are shown on the IRX–β(*GALEX*) diagram in Figure 10. Although the median position of the interacting population has redder β (median 0.0 versus −0.19) and larger IRX (2.01 versus 1.86) than the non-interacting population, the two populations are consistent with being drawn from the same distribution. The galaxies with the lowest IRX are predominantly interacting, and these systems are among the most UV-luminous sources in the GOALS sample with $\log(L_{\rm FUV}/L_{\odot}) \gtrsim 10$.

UVLGs are an interesting type of object to compare with (U)LIRGs since they are objects with extremely high SFR but little dust obscuration. Five LIRGs in our sample are also UVLGs or near-UVLGs ($L_{\rm FUV} \geqslant 10^{10.2}\ L_{\odot}$): Arp 256, VV 114, Arp 240, NGC 6090, and CGCG 448-020. The stellar masses of these systems range from $11.1 \leqslant \log(M_{\rm stellar}/M_{\odot}) \leqslant 11.5$. SFRs derived from the combination of UV and IR luminosities range from $1.8 \leqslant \log(\frac{\rm SFR}{M_{\odot}\ {\rm yr}^{-1}}) \leqslant 2.2$, and SSFRs range from $-9.6 \leqslant \log({\rm SSFR/yr}^{-1}) \leqslant -8.9$. The sample of Heckman et al. (2005) is divided into Large UVLGs and Compact UVLGs, which have mass ranges of $10.5 \leqslant \log(M_{\rm stellar}/M_{\odot}) \leqslant 11.1$ and $9.5 \leqslant \log(M_{\rm stellar}/M_{\odot}) \leqslant 10.7$, respectively, SFR ranges of $0.6 \leqslant \log(\frac{\rm SFR}{M_{\odot}\ {\rm yr}^{-1}}) \leqslant 1.2$ and $0.6 \leqslant \log(\frac{\rm SFR}{M_{\odot}\ {\rm yr}^{-1}}) \leqslant 1.4$, respectively, and SSFR ranges of $-10.5 \leqslant \log({\rm SSFR/yr}^{-1}) \leqslant -9.5$ and $-9.8 \leqslant \log({\rm SSFR/yr}^{-1}) \leqslant -8.6$, respectively. The LIRG UVLGs have larger stellar masses and considerably higher SFR than either the Large or Compact UVLG samples as a whole. The LIRG UVLGs have similar SSFR to the Compact UVLG sample, the latter group being considered as local analogs to high-redshift Lyman break galaxies (LBGs; see Overzier et al. 2009).

4.2. Optical and UV-selected (U)LIRG Samples

Figures 3 and 4 show that, on average, (U)LIRGs with high SSFR have larger IRX and IR/UV and redder β than (U)LIRGs with lower SSFR, implying greater extinction by dust in the high SSFR systems. The GOALS sample spans the same range of SSFR as the UV-selected sample of Buat et al. (2009). However the UV-selected sample does not include galaxies with high IRX ($\log({\rm IRX}) \gtrsim 2.0$), which comprise 48% of the GOALS sample. The LIRGs in the LBG sample of Buat et al. (2009) include some systems similar to the GOALS UVLGs, while the majority have higher $L_{\rm UV}$ and low IRX.

The inverse of SSFR provides a doubling timescale for the stellar mass of a galaxy. The range for GOALS systems (excluding those with IRAC colors suggesting a possible AGN) is from 18 Gyr to 290 Myr, with a median of 2.6 Gyr. Kaviraj (2009) fit double-burst star formation history models to a large sample of SDSS-selected LIRGs out to $z = 0.2$, finding average burst ages of 7 Gyr and 1 Gyr. The 43 systems in common between Kaviraj (2009) and the GOALS *GALEX* sample are consistent with being drawn from the same distribution in β and IRX as the entire GOALS *GALEX* sample.

4.3. Resolved Systems and Implications for Unresolved LIRGs at High Redshift

As emphasized by Charmandaris et al. (2004), individual galaxies in interacting systems can have very different far-infrared and UV properties leading to incorrect assumptions about the system as a whole when viewed as a single unresolved system (e.g., at high redshift). In particular, these authors note that the mid-IR/UV ratios of the components of the Arp 299 and VV 114 systems vary by well over an order of magnitude between the individual interacting galaxies. Our combined *GALEX* and *Spitzer* observations of the GOALS sample show that this situation exists in a significant number of LIRG systems at low redshift. We define a source that produces at least twice as much luminosity as the companion to be dominant at that wavelength. Among LIRGs which can be resolved into interacting galaxies, approximately 32% consist of one galaxy which dominates the IR luminosity while a companion dominates the UV (hereafter referred to as "VV 114-like" systems). Extrapolating to number counts at $z \geqslant 1$ as in Charmandaris et al. (2004), this implies that as many as 15%–30% of high-redshift galaxies are unresolved VV 114-like systems.

In 21% of resolved systems, a single galaxy dominates both the IR and UV emission (such as Arp 182, for example). On average, the ΔIRX value of the dominant galaxy is over four times larger than that of IR-dominant galaxies of similar UV color in a VV 114-like system. If we look at the masses of resolved pairs, the ΔIRX of the more massive galaxy is on average four times greater than that of the less massive galaxy. These are independent effects: the IR-dominant galaxy in a resolved system is likely to dominate the mass of the system regardless of its contribution to the UV luminosity of the system. If we make the simplistic assumption that LIRG mergers form a single evolutionary sequence, our observations suggest that the phase in which the component galaxies have comparable IR and UV emission is 50% longer than the phase in which a single galaxy dominates both wavelengths. Furthermore, the fact that the high mass component is above the starburst relation would also be consistent with the fact that a synchronization of the nuclear starbursts in the two interacting galaxies is rare.

The ability to visualize merger simulations at observed wavelengths from the FUV to the FIR will facilitate the interpretation of data sets such as that presented in this paper. The SUNRISE code of Jonsson et al. (2006) may help answer outstanding questions such as: what types of mergers (and what

fraction of viewing orientations) consist of an IR-dominant LIRG with a UV-dominant companion? What mergers consist of an LIRG which dominates both IR and UV relative to its companion? How long do these phases last? Do certain types of progenitor galaxies (Hubble type, mass ratio, gas fraction, orbit, etc.) lead to different observables (IRX, β(*GALEX*), IR or UV fraction, SSFR, etc.) during the merger?

Although the different definitions of β(*GALEX*) preclude a direct comparison, the GOALS sample appears to be generally consistent with the merger simulations shown in Jonsson et al. (2006). In particular, the ULIRG simulations predict an IRX that is up to a factor of 10 times greater than starburst galaxies with a narrow range of blue to intermediate UV colors. The GOALS ULIRGs within the same range of β(*IUE*) have a median ΔIRX of 0.9.

5. CONCLUSIONS

We present a comparison of the UV and infrared properties of 135 LIRGs and ULIRGs in the GOALS sample observed by *GALEX* and *Spitzer*. We find that

1. LIRGs have larger IR excesses than lower luminosity galaxies of similar UV color. On average, more luminous LIRGs and ULIRGs have larger IRX and redder colors.
2. The contribution of the FUV to the measured SFR is on average 4%; UV emission alone is not a reliable indicator of the SFR for LIRGs.
3. The median SSFR of the GOALS sample (3.9×10^{-10} yr^{-1}, corresponding to a mass doubling timescale of 2.6 Gyr) is approximately equal to the maximum SSFR seen in lower luminosity galaxies; however, the median IR/UV ratio (39) for GOALS galaxies is more than an order of magnitude greater.
4. Deviations from the starburst IRX–β(*GALEX*) relation ΔIRX increase with IR luminosity for $L_{\rm IR} \gtrsim 10^{10}\ L_{\odot}$, with considerable scatter. LIRG systems with IRAC colors that may indicate the presence of an AGN have average IRX ratios a factor of 6 larger than the rest of the sample. ΔIRX is not strongly correlated with *IRAS* 25 μm/60 μm color, *IRAS* 60 μm/100 μm color, *Spitzer* 8 μm/24 μm color, $L_{\rm FUV}$, or 8 μm concentration (1 kpc/total).
5. A minimum of 19% of the total $L_{\rm IR}$ of the RBGS sample is produced in LIRGs and ULIRGs with $\beta > 0$, sources that are typically absent from UV-selected samples at high redshift. A minimum of 11% of the total $L_{\rm IR}$ of the RBGS sample is produced in LIRGs and ULIRGs with ΔIRX > 1, an order of magnitude above the starburst relation.
6. Using the starburst IRS–β relation to estimate $L_{\rm IR}$ from rest-frame UV observations of LIRGs and ULIRGs would underestimate $L_{\rm IR}$ by a factor of 3 on average, with a wide range (factors of 0.2–68) of possible under- or overestimates, particularly for red UV colors (large values of β) where $L_{\rm IR}$ could be overestimated by as much as a factor of 2400 using a linear extrapolation of the starburst relation.
7. The UV and IR properties of GOALS systems are qualitatively consistent with an evolutionary picture in which some galaxies transition from LIRGs to ULIRGs over the course of a major merger event. More luminous galaxies, mergers, and galaxies with high SSFR are more heavily obscured than less luminous galaxies, non-mergers, and galaxies with lower SSFR.
8. Among LIRG systems resolved into individual interacting galaxies, pairs in which one galaxy dominates the IR emission while the companion dominates UV emission (such as the well-studied LIRG system VV 114) are more common than pairs in which one galaxy dominates both wavelengths (32% and 21% of the sample, respectively). On average, galaxies which dominate both wavelengths have ΔIRX values four times larger than an IR-dominant galaxy in a "VV 114-like" system. The large fraction of "VV 114-like" systems has important implications for observations of interacting galaxies at high redshift in that the IR and UV properties of the unresolved systems can differ by over an order of magnitude from the properties of the component galaxies.

This research has made use of the NASA/IPAC Extragalactic Database (NED) which is operated by the Jet Propulsion Laboratory, California Institute of Technology, under contract with the National Aeronautics and Space Administration. This research has made use of the NASA/IPAC Infrared Science Archive, which is operated by the Jet Propulsion Laboratory, California Institute of Technology, under contract with the National Aeronautics and Space Administration. Based on observations made with the NASA Galaxy Evolution Explorer. *GALEX* is operated for NASA by the California Institute of Technology under NASA contract NAS5-98034. V.C. acknowledges partial support from the EU ToK grant 39965 and FP7-REGPOT 206469. We thank Ranga Chary, Brian Siana, and Harry Teplitz for helpful discussions. We thank Armando Gil de Paz for making his *GALEX* background subtraction code available, Danny Dale for providing the SINGS data points in Figure 3, and the anonymous referee for helpful comments.

APPENDIX

UV COLORS

The UV color of an object can be parameterized in several ways, complicating the comparison of results between different data sets. The UV continuum slope β was defined by Calzetti et al. (1994) for use with *IUE* spectra. More recent photometric instruments such as STIS (Goldader et al. 2002) and *GALEX* cannot directly measure this spectroscopic β, referred to as β(*IUE*) in the main text of this paper and in Figure 1. Instead, the slope between an NUV data point and an FUV data point is measured and labeled β, referred to as β(*GALEX*). Some authors abandon the UV slope and instead measure a conventional color FUV–NUV, expressed in magnitudes (e.g., GDP).

Since 11 galaxies from Meurer et al. (1999) are included in GDP, we derive an empirical conversion between β(*IUE*) and β(*GALEX*):

$$\beta(IUE) = (-0.3 \pm 0.1) + (1.6 \pm 0.2)\beta(GALEX). \quad \text{(A1)}$$

This conversion is not necessarily valid outside the range $-2 < \beta(IUE) < 0.5$ or $-1 < \beta(GALEX) < 0.5$.

REFERENCES

Armus, L., et al. 2009, PASP, 121, 559
Boquien, M., et al. 2009, ApJ, 706, 553
Buat, V., Takeuchi, T. T., Burgarella, D., Giovannoli, E., & Murata, K. L. 2009, A&A, 507, 693
Calzetti, D., Kinney, A. L., & Storchi-Bergmann, T. 1994, ApJ, 429, 582

Caputi, K. I., Dole, H., Lagache, G., McLure, R. J., Dunlop, J. S., Puget, J.-L., Le Floc'h, E., & Pérez-González, P. G. 2006, A&A, 454, 143
Charlot, S., & Fall, S. M. 2000, ApJ, 539, 718
Charmandaris, V., Le Floc'h, E., & Mirabel, I. F. 2004, ApJ, 600, L15
Charmandaris, V., Stacey, G. J., & Gull, G. 2002, ApJ, 571, 282
Cortese, L., et al. 2006, ApJ, 637, 242
Dale, D. A., et al. 2007, ApJ, 655, 863
de Vaucouleurs, G., de Vaucouleurs, A., Corwin, H. G., Jr., Buta, R. J., Paturel, G., & Fouque, P. 1991, Third Reference Catalogue of Bright Galaxies, Vols. 1–3, XII (Berlin: Springer)
Genzel, R., Tacconi, L. J., Rigopoulou, D., Lutz, D., & Tecza, M. 2001, ApJ, 563, 527
Gil de Paz, A., et al. 2007, ApJS, 173, 185 (GDP)
Goldader, J. D., Meurer, G., Heckman, T. M., Seibert, M., Sanders, D. B., Calzetti, D., & Steidel, C. C. 2002, ApJ, 568, 651
Heckman, T. M., et al. 2005, ApJ, 619, L35
Jonsson, P., Cox, T. J., Primack, J. R., & Somerville, R. S. 2006, ApJ, 637, 255
Kaviraj, S. 2009, MNRAS, 394, 1167
Kennicutt, R. C., Jr. 1998, ARA&A, 36, 189
Kennicutt, R. C., Jr., et al. 2003, PASP, 115, 928
Kong, X., Charlot, S., Brinchmann, J., & Fall, S. M. 2004, MNRAS, 349, 769
Lacey, C. G., Baugh, C. M., Frenk, C. S., Silva, L., Granato, G. L., & Bressan, A. 2008, MNRAS, 385, 1155
Le Floc'h, E., et al. 2005, ApJ, 632, 169
Leitherer, C., et al. 1999, ApJS, 123, 3
Magnelli, B., Elbaz, D., Chary, R. R., Dickinson, M., Le Borgne, D., Frayer, D. T., & Willmer, C. N. A. 2009, A&A, 496, 57
Magorrian, J., et al. 1998, AJ, 115, 2285
Meurer, G. R., Heckman, T. M., & Calzetti, D. 1999, ApJ, 521, 64
Muñoz-Mateos, J. C., et al. 2009, ApJ, 701, 1965
Overzier, R. A., et al. 2009, ApJ, 706, 203
Salpeter, E. E. 1955, ApJ, 121, 161
Sanders, D. B., Mazzarella, J. M., Kim, D.-C., Surace, J. A., & Soifer, B. T. 2003, AJ, 126, 1607
Sanders, D. B., & Mirabel, I. F. 1996, ARA&A, 34, 749
Sanders, D. B., Soifer, B. T., Elias, J. H., Madore, B. F., Matthews, K., Neugebauer, G., & Scoville, N. Z. 1988a, ApJ, 325, 74
Sanders, D. B., Soifer, B. T., Elias, J. H., Neugebauer, G., & Matthews, K. 1988b, ApJ, 328, L35
Seibert, M., et al. 2005, ApJ, 619, L55
Stern, D., et al. 2005, ApJ, 631, 163
Surace, J. A., & Sanders, D. B. 2000, AJ, 120, 604
Surace, J. A., Sanders, D. B., & Evans, A. S. 2000, ApJ, 529, 170
Tacconi, L. J., Genzel, R., Lutz, D., Rigopoulou, D., Baker, A. J., Iserlohe, C., & Tecza, M. 2002, ApJ, 580, 73
Wyder, T. K., et al. 2005, ApJ, 619, L15